Measurement of the Forward-Backward Asymmetry in Gamma/Z boson to Dilepton Events in Compact Muon Solenoid at a Center-of-mass Energy of 7 TeV

by

Youn Jung Roh

A Dissertation

In

PHYSICS

Submitted to the Graduate Faculty
of Texas Tech University in
Partial Fulfillment of
the Requirements for
the Degree of

DOCTOR OF PHILOSOPHY

Approved

Nural Akchurin
Chair of Committee

Dan Green

Sung-Won Lee

Mahdi Sanati

Richard Wigmans

Peggy Gordon Miller
Dean of the Graduate School

December, 2011

Copyright 2011, Youn Jung Roh

Acknowledgments

I would like to express my gratitude to many people who made this thesis possible. First of all, I would like to thank my advisor, Nural Akchurin, who guided me a right path in a graduate studies. He taught me not just the high energy physics but also the way to spend my life wisely. I owe a great gratitude to John Hauptman who introduced me Nural.

I am also grateful to my colleagues who are involved in the forward/backward asymmetry, Sung-won Lee, Efe Yazgan, Kittikul Kovitanggoon, Dan Green, Arie Bodek, Jiyeon Han, and Yeonsei Chung. This thesis would not exist without their support and help. Specially, I would like to show my deepest gratitude to Yeonsei Chung who encouraged me to be a physicist when I lost the track.

I want to thank to Texas Tech high energy group and the Department of physics for supporting me in my research work. I must thank to Suvadeep Bose, Jason St. John, and Kathy Gillis, for getting this thesis into better shape. Finally, I thank my family for their support and devotion to me.

Contents

Acknowledgments **ii**

Abstract **vi**

List of Tables **vii**

List of Figures **x**

1 Introduction **1**

2 Theory **3**

2.1 Electroweak Theory of the Standard Model 3

2.2 The Forward-Backward Asymmetry 4

2.3 The Collins-Soper Frame 6

3 Apparatus **8**

3.1 The Large Hadron Collider (LHC) 8

3.2 Compact Muon Solenoid (CMS) 9

3.2.1 The Superconducting Magnet 10

3.2.2 The Inner Tracker 10

3.2.3 The Electromagnetic Calorimeter (ECAL) 11

3.2.4 The Hadron Calorimeter (HCAL) 13

3.2.5 The Muon System 15

4 Data Set and Event Selection **17**

4.1 Data Set 17

4.2 Electron Selection 18

4.2.1 Electron Selection in Central Region 18

4.2.2 Electron Selection in Forward Region 19

4.3 Muon Selection 20

4.4 Lepton Pair Selection 21

5 Corrections **23**

5.1 Energy Scale and Resolution 23

5.1.1 Electron in Central Region 23

5.1.2 Electron in Forward Region 24

5.1.3 Muons 27

5.2 Pile-up 29

5.3 Electron and Muon Identification Efficiencies in Central Region 31

6 Background **34**

6.1 Backgrounds in Central Region 34

6.2 Background in the Forward Region 37

7 Results **39**

7.1 Distribution 39

7.2 Raw A_{FB} 39

7.2.1 Raw A_{FB} measured in Central Region 39

7.2.2 Raw A_{FB} measured in the Forward Region 41

7.3 Unfolding 43

7.3.1 Dilution Effects 43

7.3.2 Unfolding Procedure 44

7.3.3 Limited Pre-FSR A_{FB} Stage 45

7.3.4 Full Pre-FSR A_{FB} Stage 48

7.3.5 A_{FB}, $|y| > 1$ 48

7.3.6 Non-diluted A_{FB} 51

8 Systematics **59**

8.1 Pile-up 59

8.2 Efficiency 60

8.3 Energy Scale and Resolution 60

8.3.1 Electron 60

8.3.2 Muon 61

8.4 Background 62

8.5 Response Matrices 63

8.6 P_{T} of Dilepton 63

8.7 Quantum Electrodynamics (QED) Final State Radiation (FSR) 63

8.8 Mis-alignment 65

8.9 Parton Distribution Functions (PDFs) 68

9 Conclusion **69**

Abstract

The forward-backward asymmetry parameter (A_{FB}) as a function of dilepton invariant mass in $Z/\gamma^* \to l^+l^-$ (l=e or μ) at $\sqrt{s}$=7 TeV is measured using 2.2 fb^{-1} of pp collision data in 2011. The forward-backward asymmetry measurement is performed using muons within $|\eta| < 2.1$ and electrons within $|\eta| < 2.4$ in a wide mass range between 40 GeV/c^2 to 1000 GeV/c^2. The forward-backward asymmetry is also measured for the first time in a large rapidity range of $|\eta| < 5$ with electrons using the CMS forward calorimeters and results in a less diluted A_{FB} measurement, as expected. The forward-backward asymmetry parameters are unfolded in three stages, limited pre-FSR, full pre-FSR, and non-diluted stage in order to obtain parton level A_{FB}. The muon and electron results are combined, and the individual and combined results are found to be consistent with the Standard Model prediction within statistical and systematic uncertainties.

List of Tables

1.1 The Standard Model describes the nature and their interactions by three generations of quarks and leptons and four gauge bosons. 1

2.1 The weak isospin and charge of fermions is listed. 4

3.1 The summary of LHC parameters for operation in 2011 [26]. 9

4.1 All data were collected in 2011 at $\sqrt{s} = 7$ TeV and amounts to 2.2 fb^{-1}. . . 18

4.2 Monte Carlo signal and background samples are listed with integrated luminosity in pb^{-1}. 18

4.3 WP80 selection criteria. Note that the ECAL energy corrections are not applied to the E_{T} and H/E ratio used in this analysis*. 19

4.4 Muon selection criteria [13]. 21

5.1 The ECAL energy scale factors applied in data in the electron channel. . . . 29

5.2 The ECAL energy smearing factors applied in MC in the electron channel. . 29

5.3 The energy scale and resolution correction factors in HF+ and HF-. 31

5.4 The signal and background MCs are tuned to account for pile-up by the weighting factors. 32

5.5 Electron identification efficiency. The ratios of data to MC efficiency are given. 33

5.6 Muon identification efficiency. The ratios of data to MC efficiency are given. 33

6.1 The numbers of background events in central region are estimated in 2.2 fb^{-1} of the integral luminosity. 37

6.2 The numbers of background events are estimated in 2.2 fb^{-1} of the integral luminosity. The listed numbers of backgrounds fake the central and forward electron pairs. 38

7.1 The numerical values for the raw A_{FB} (central electron) are listed. 43

7.2 The numerical values for the raw A_{FB} for dimuon are listed. 44

7.3 Unfolded A_{FB} to limited pre-FSR electron stage in electron. 51

7.4 Unfolded A_{FB} to limited pre-FSR electron stage in muon. 52

7.5 The statistical error comparison is shown in the electron and muon channels. N_i is observed events here. 53

7.6 Unfolded A_{FB} to pre-FSR stage with acceptance correction for electron. . . 54

7.7 Unfolded A_{FB} to pre-FSR stage with acceptance correction for muon. 55

7.8 Dilution rates of D_{BF} and D_{FB} in the electron and muon channels. 56

8.1 The energy scale and resolution correction with respect to η bins. 62

8.2 The re-weighting factors for MC tuning on P_{T} of dilepton in the electron and muon channel. 65

8.3 The muon momentum correction parameters using the MuScleFit algorithm [60]. 66

8.4 Systematic error in the electron channel is listed in order of invariant mass of dimuon, pile-up (Pileup), efficiency (Effi), energy scale (Ecale), energy smearing (Eres), background (Bk), Response matrices (Mat), Transverse momentum of dilepton ($P_{\text{T}}^{e^+e^-}$), QED FSR (FSR), and total systematic error (Sys.E). 68

8.5 Systematic error in the muon channel is listed in order of invariant mass of dimuon, pile-up (Pileup), efficiency (Effi), energy scale (Ecale), energy smearing (Eres), background (Bk), Response matrices (Mat), Transverse momentum of dilepton ($P_{\mathrm{T}}^{\mu^+\mu^-}$), QED FSR (FSR), mis-alignment (Mis), and total systematic error (Sys.E). 68

List of Figures

2.1 The Feynman diagram for Drell-Yan process [22]. 4

3.1 The figure shows the overall view of the LHC experiments [25]. 8

3.2 The overall layout of the CMS detector. 10

3.3 The overview of the tracker layout. 11

3.4 The isometric view of the ECAL calorimeter. 12

3.5 The schematic view of HCAL calorimeter. 13

3.6 a) Transverse segmentation of the HF towers are shown. b) An expanded view of the wedge is illustrated [38]. 14

3.7 The cross sectional view of the HF. 15

4.1 A typical electron (100 GeV) shower in the forward calorimeter (by Nural Akchurin and Ken Carrell). 20

4.2 A typical proton (100 GeV) shower in the forward calorimeter (by Nural Akchurin and Ken Carrell). 20

5.1 Transverse energy of electron with respect to 10 different η bins in data and MC. 25

5.2 Transverse energy of muon in 10 η bins. 26

5.3 The invariant mass of dielectron (top) and the ratio between data and MC varies from 0.8 to 1.4 (bottom). 27

5.4 The invariant mass dimuons (top) and the ratio between data and MC varies from 0.9 to 1.1 (bottom). 27

5.5 The dielectron invariant mass comparison between data and MC before the energy scale and resolution correction applied. 28
5.6 The invariant mass of dielectron in data and MC is corrected by energy scale and resolution correction factors. The maximum energy scale factor is about 1.05 for data, and the maximum energy smearing factor for MC is about 0.04. 28
5.7 The invariant mass distribution of dielectrons is shown without the energy scale and resolution corrections. The peak of invariant mass in data is about 5 GeV$/c^2$ off from that of simulation. 30
5.8 The invariant mass distribution of dielectrons with energy scale and resolution corrections. The bottom plot shows the ratio of data to MC, displaying the level of tuning between the two. 30
5.9 The number of vertices of the electron channel. 30
5.10 The number of vertices of the muon channel. 30

6.1 The invariant mass of same-signed dimuon event in data and signal MC. 35
6.2 The invariant mass of same-signed dielectron event in data and signal MC. 35
6.3 Invariant mass difference of same-signed dielectrons between data and MC. 35
6.4 Charge mis-identification rates for electron pairs. 36
6.5 The MC QCD mass shape is shown. To increase statistics loose selection cut (WP95) and anti-isolation are used. 36
6.6 The invariant mass distribution in the electron channel. 37
6.7 The invariant mass distribution in the muon channel. 37
6.8 Invariant mass distributions where one electron is in the central and the second is in the forward regions. 38

7.1 The corrected P_{T} (top left), $M_{e^+e^-}$ (top right), $\cos\theta^*$ (bottom left), and rapidity distribution (bottom right) of dielectron are shown. 40

7.2 The corrected P_{T} (top left), $M_{\mu^+\mu^-}$ (top right), $\cos\theta^*$, (bottom left) and rapidity distribution (bottom right) of dimuon are shown. 40

7.3 The raw A_{FB} is shown based on dielectrons in the central region. The blue solid line is the expected the A_{FB}, and the black circles are data with statistical errors. 41

7.4 The raw A_{FB} is shown based on dimuons in the central region. The solid line in blue is the expected the A_{FB}, and the black circles are data with statistical errors. 41

7.5 The corrected P_{T} (top left), M_{ee} (top right), $\cos\theta^*$ (bottom left), and rapidity distribution (bottom right) of central and forward electron are shown. 42

7.6 The raw A_{FB} with a central and forward electron pair. The statistical errors are in red and the combined statistical and systematic errors are in black. Background subtraction and the energy scale are considered to define systematic errors. 42

7.7 The born level of Drell-Yan process with FSR. 43

7.8 Response matrices in the electron channel. 46

7.9 Response matrices in the muon channel. 46

7.10 Closure test in the electron channel. 47

7.11 Unfolded A_{FB} to the limited pre-FSR electron stage. 48

7.12 Unfolded A_{FB} to limited pre-FSR muon stage. 48

7.13 A_{FB} is tested in 12 mass regions with 1000 pseudo-experimental toys to evaluated the statistical errors. 49

7.14 The response matrices are normalized by all generated events in order to unfold to full pre-FSR stage in the electron channel. 50

7.15 Response matrices are normalized by all generated events in order to unfold to full pre-FSR stage in the muon channel. 50

7.16 The inversion process for unfolding to all pre-FSR stage is checked by a closure test with reconstructed electron in MC. 53
7.17 Unfolded A_{FB} to all pre-FSR electron stage. 54
7.18 Unfolded A_{FB} to all pre-FSR muon stage. 54
7.19 Unfolding A_{FB} to limited pre-FSR stage in the electron channel with $|y| > 1$ cut. . . 55
7.20 Unfolding A_{FB} to limited pre-FSR stage in the muon channel with $|y| > 1$ cut. . . . 55
7.21 Unfolding A_{FB} to all pre-FSR stage in the electron channel with $|y| > 1$ cut. 56
7.22 Unfolding A_{FB} to all pre-FSR stage in the muon channel with $|y| > 1$ cut. 56
7.23 Closure test in the electron channel for unfolding to non-diluted stage. . . . 57
7.24 Unfolded A_{FB} to non-diluted stage in the electron channel. 57
7.25 Unfolded A_{FB} to non-diluted stage in the muon channel. 57
7.26 Unfolded A_{FB} to non-diluted stage in the lepton channel. 58

8.1 Systematic uncertainty of pile-up in the electron channel. 59
8.2 Systematic uncertainty of efficiency in the electron channel. 60
8.3 Systematic uncertainty of energy scale in the electron channel. 61
8.4 Systematic uncertainty of energy scale in the muon channel. 61
8.5 Systematic uncertainty of energy resolution in the electron channel. 61
8.6 Systematic uncertainty of energy resolution in the muon channel. 61
8.7 Systematic uncertainty of background subtraction in the electron channel. . 62
8.8 Systematic uncertainty of response matrices in the electron channel. 63
8.9 Systematic uncertainty of P_{T} of dilepton in the electron channel. 64
8.10 Energy difference between before and after QED FSR. 64
8.11 Systematic uncertainty of FSR in the electron channel. 66
8.12 Systematic uncertainty of mis-alignment in the muon channel. 67
8.13 Invariant mass in data and MC with the MuScleFit correction. 67

Chapter 1

Introduction

The Standard Model (SM) [1, 2] describes the elementary particles and the nature of their interaction such as the electromagnetic, weak, and strong nuclear interactions [3]. The SM, formulated in the mid 1970s, posits that matter is made of six quarks and six leptons, and their interactions are mediated by four gauge bosons listed in Table 1.1 [4]. The discoveries of the bottom quark in 1977 [5], the top quark in 1995 [6], and the tau neutrino in 2000 [7] support the SM by revealing the existence of three generations of quarks and leptons. Furthermore, the observations of W and Z boson in 1983 are evidence in favor of the SM [8, 9].

Table 1.1: The Standard Model describes the nature and their interactions by three generations of quarks and leptons and four gauge bosons.

Fermions	1st Generation	2nd Generation	3rd Generation	Gauge bosons
Quarks	u (Up quark)	c (Charm quark)	t (Top quark)	γ (Photon)
	d (Down quark)	s (Strange quark)	b (Bottom quark)	g (Gluon)
Leptons	e (Electron)	μ (Muon)	τ (Tau)	Z
	ν_e (Electron neutrino)	ν_μ (Muon neutrino)	ν_τ (Tau neutrino)	W

The SM, however, is known to be incomplete [10]. In this thesis, the SM is further tested at $\sqrt{s}$=7 TeV by a precision measurement, the forward-backward asymmetry (A_{FB}) [11, 12, 13, 14, 15, 16] using the CMS detector.

We largely adopt the Tevatron's A_{FB} analysis technique [17, 18]. Performing the same measurement, however, is more difficult at the LHC. At the Tevatron, the proton collides with the anti-proton and the quark (anti-quark) direction can be determined most of the

time. Identifying the quark (anti-quark) direction at the LHC is not simple because both beams are composed of protons. Therefore, the A_{FB} measurement at the LHC requires more care. In this thesis, the details of this measurement and the analysis techniques are described.

One of the unique aspects of the CMS detector is that the electrons can be detected up to $|\eta| < 5$ with good efficiency which enables us to measure a less diluted asymmetry.

Chapter 2

Theory

2.1 Electroweak Theory of the Standard Model

The standard electroweak model is based on the gauge group SU(2)×U(1) [19]. In the SM, the electroweak Lagrangian is written as $\mathscr{L} = \mathscr{L}_{\text{Higgs}} + \mathscr{L}_{\text{Symm}}$. The first term, $\mathscr{L}_{\text{Higgs}}$ explains the massive gauge boson by the electroweak symmetry breaking with the existence of the massive spin zero particle, Higgs boson [20]. The second term, $\mathscr{L}_{\text{Symm}}$ describes the fermion fields and their electroweak interactions.

The Lagrangian $\mathscr{L}_{\text{Symm}}$ for the fermion field has the following vertex term for the Z boson and a fermion pair.

$$-\frac{g}{2\cos\theta_W}\sum_i \overline{\psi_i}\gamma^\mu(g_{\text{V}}^i - g_{\text{A}}^i\gamma^5)\psi_i Z_\mu \tag{2.1}$$

where the weak angle $\theta_W = \tan^{-1}(g\prime/g)$, g and $g\prime$ are gauge coupling constants of SU(2) and U(1) respectively, and $e = g\cos\theta_W$ is the positron electric charge. The vector and axial-vector coupling are

$$g_{\text{V}}^i = t_{3L}(i) - 2q_i\sin^2\theta_W, \tag{2.2}$$

$$g_{\text{A}}^i = t_{3L}(i). \tag{2.3}$$

where $t_{3L}(i)$ is the weak isospin of fermion i, and q_i is the charge of ψ_i in units of e. (see Table 2.1)

Table 2.1: The weak isospin and charge of fermions is listed.

Fermion i	$t_{3L}(i)$	q_i
ν_e, ν_μ, ν_τ	$\frac{1}{2}$	0
e, μ, τ	$-\frac{1}{2}$	-1
u, c, t	$\frac{1}{2}$	$\frac{2}{3}$
d, s, b	$-\frac{1}{2}$	$-\frac{1}{3}$

2.2 The Forward-Backward Asymmetry

The Drell-Yan process [21], $q\bar{q} \to Z/\gamma^* \to l^+l^-$, proceeds through an s-channel exchange of either a virtual photon or a Z boson at born level. (see Figure 2.1)

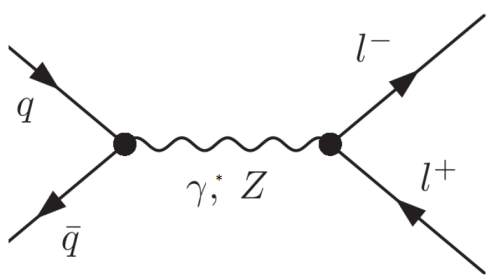

Figure 2.1: The Feynman diagram for Drell-Yan process [22].

The forward-backward asymmetry (A_{FB}) originates from the presence of both vector and axial-vector coupling of electroweak bosons to fermions in $q\bar{q} \to Z/\gamma^* \to l^+l^-$ process. Due to the vector and axial-vector coupling, an asymmetry is present in the polar angle between the lepton and incoming quark in the rest frame of the lepton pair. The differential cross-section for the parton level process in terms of the lepton scattering angle θ is following [17].

$$\begin{aligned}\frac{d\sigma(q\bar{q} \to l^+l^-)}{d\cos\theta} &= C\frac{\pi\alpha^2}{2s}\{q_l^2 q_q^2(1+\cos^2\theta) \\ &\quad + q_l q_q Re[\chi(s)][2g_{\mathrm{V}}^q g_{\mathrm{V}}^l(1+\cos^2\theta) + 4g_{\mathrm{A}}^q g_{\mathrm{A}}^l \cos\theta]\end{aligned}$$

$$+|\chi(s)|^2[(g_{\mathrm{V}}^{q2}+g_{\mathrm{A}}^{q2})\times(g_{\mathrm{V}}^{l2}+(g_{\mathrm{A}}^{l2})(1+\cos^2\theta)$$
$$+8g_{\mathrm{V}}^{q}g_{\mathrm{A}}^{q}g_{\mathrm{V}}^{l}g_{\mathrm{A}}^{l}\cos\theta]\} \tag{2.4}$$

where C is the color factor, θ is the emission angle between the lepton (antilepton) and the quark (antiquark) in the rest frame of the lepton pair, and $q_{l,q}$ is the charge of the lepton or quark, s is the center-of-mass energy squared of the incoming $q\bar{q}$ system, and $\chi(s)$ is

$$\chi(s)=\frac{1}{\cos^2\theta_W\sin^2\theta_W}\frac{s}{s-M_Z^2+i\Gamma_Z M_Z}. \tag{2.5}$$

The differential cross section in Equation (2.4) simplifies to

$$\frac{d\sigma}{d(\cos\theta)}=A(1+\cos^2\theta)+B\cos\theta \tag{2.6}$$

where θ is the emission angle of the electron relative to the quark momentum in the center-of-mass frame of the dilepton. A and B parameters which depend on the weak isospin and charge of the incoming fermions are:

$$\begin{aligned} A &= q_l^2q_q^2+2q_lq_qg_{\mathrm{V}}^{q}g_{\mathrm{V}}^{l}Re[\chi(s)]+g_{\mathrm{V}}^{l2}(g_{\mathrm{V}}^{q2}+g_{\mathrm{A}}^{q2})|\chi(s)|^2+g_{\mathrm{A}}^{l2}(g_{\mathrm{V}}^{q2}+g_{\mathrm{A}}^{q2})|\chi(s)|^2, \\ B &= \frac{3}{2}g_{\mathrm{A}}^{q}g_{\mathrm{A}}^{l}[q_lq_qRe[\chi(s)]+2g_{\mathrm{V}}^{q}g_{\mathrm{V}}^{l}|\chi(s)|^2]. \end{aligned} \tag{2.7}$$

The $\cos\theta$ terms in Equation (2.4) introduce the forward-backward asymmetry, and the A_{FB} is written in cross section of the forward (σ_{F}) and backward events (σ_{B}) as:

$$\begin{aligned} A_{\mathrm{FB}} &= \frac{\int_0^1\frac{d\sigma}{d(\cos\theta)}d(\cos\theta)+\int_{-1}^0\frac{d\sigma}{d(\cos\theta)}d(\cos\theta)}{\int_{-1}^1\frac{d\sigma}{d(\cos\theta)}d(\cos\theta)} \\ &= \frac{\sigma_{\mathrm{F}}-\sigma_{\mathrm{B}}}{\sigma_F+\sigma_B} \end{aligned} \tag{2.8}$$

where

$$\begin{aligned}
\sigma_{\mathrm{F}} &= \int_0^1 \frac{d\sigma}{d(\cos\theta)} d(\cos\theta) = A\left(1+\frac{1}{3}\right) + B\left(\frac{1}{2}\right), \\
\sigma_{\mathrm{B}} &= \int_{-1}^0 \frac{d\sigma}{d(\cos\theta)} d(\cos\theta) = A\left(1+\frac{1}{3}\right) - B\left(\frac{1}{2}\right), \\
A_{\mathrm{FB}} &= \frac{\sigma_{\mathrm{F}} - \sigma_{\mathrm{B}}}{\sigma_F + \sigma_B} = \frac{3B}{8A}.
\end{aligned} \tag{2.9}$$

As a result, the A_{FB} tests the vector and axial-vector coupling of the electroweak interaction directly. The reaction $q\bar{q} \to l^+l^-$ is mediated primarily by virtual photons at low dilepton invariant mass (<60 GeV/c^2). Around the Z pole, it is dominated by the Z boson coupling. At heavier masses, the reaction is mediated by a combination of virtual photons and Z bosons. The asymmetry is expected to be small in the low mass region and near the Z peak, and sizable for > 110 GeV/c^2.

2.3 The Collins-Soper Frame

The forward-backward asymmetry in Equation (2.9) can be written as

$$A_{\mathrm{FB}} = \frac{N_{\mathrm{F}} - N_{\mathrm{B}}}{N_{\mathrm{F}} + N_{\mathrm{B}}} \tag{2.10}$$

where N_{F} is the number of forward events ($\cos\theta > 0$), and N_{B} is the number of backward events ($\cos\theta < 0$).

Therefore, the A_{FB} is measured by counting N_{F} and N_{B}. The determination of the forward-backward event is based on the emission angle of the lepton relative to the quark momentum in the center-of-mass frame of dilepton. Thus, defining the quark direction is

the beginning of the forward backward asymmetry measurement.

At the Tevatron (proton-antiproton collider), a proton direction is referred to a quark direction. Since LHC is proton-proton collider, the quark direction cannot be defined by a beam direction. Because sea quarks ($\bar{q}$) carry less momentum than valence quarks, we assume the dilepton system moves in the direction of the valence quark. Therefore, on average, we take the quark direction as the direction of the dilepton system at the LHC.

The next factor is to determine the scattering angle θ between the outgoing lepton and incoming quark. To minimize the effect of the transverse momentum of the incoming quark, the Collins-Soper frame [23] is used, where θ^* is defined to be the angle between the lepton momentum and the z' axis that bisects the angle between $\mathbf{p}_q$ and $-\mathbf{p}_{\bar{q}}$. Therefore,

$$\cos\theta^* = \frac{2(\ell^+\ell'^- - \ell^-\ell'^+)}{\sqrt{Q^2(Q^2+Q_{\mathrm{T}}^2)}} \tag{2.11}$$

where Q_{T} is the dilepton transverse momentum vector and

$$Q^\nu = \ell^\nu + \ell'^\nu \tag{2.12}$$

$$\ell^\nu = e^- \text{ momentum} \tag{2.13}$$

$$\ell'^\nu = e^+ \text{ momentum} \tag{2.14}$$

$$\ell^\pm = \frac{\ell^0 \pm \ell^3}{\sqrt{2}}. \tag{2.15}$$

All quantities are measured in the lab frame.

Chapter 3

Apparatus

3.1 The Large Hadron Collider (LHC)

The LHC [24] is constructed in the existing 27 km of the Large Electron Positron (LEP) tunnel at the European Organization for Nuclear Research (CERN) near Geneva, Switzerland. The LHC is designed for head-on collisions of proton beams with a center-of-mass energy of 14 TeV and a luminosity of 10^{34} cm^{-2} s^{-1}. During 2011, when this measurement is carried out, the center-of-mass energy was 7 TeV with a peak luminosity of 10^{33} cm^{-2} s^{-1}. Table 3.1 shows performance related parameters for operation in 2011.

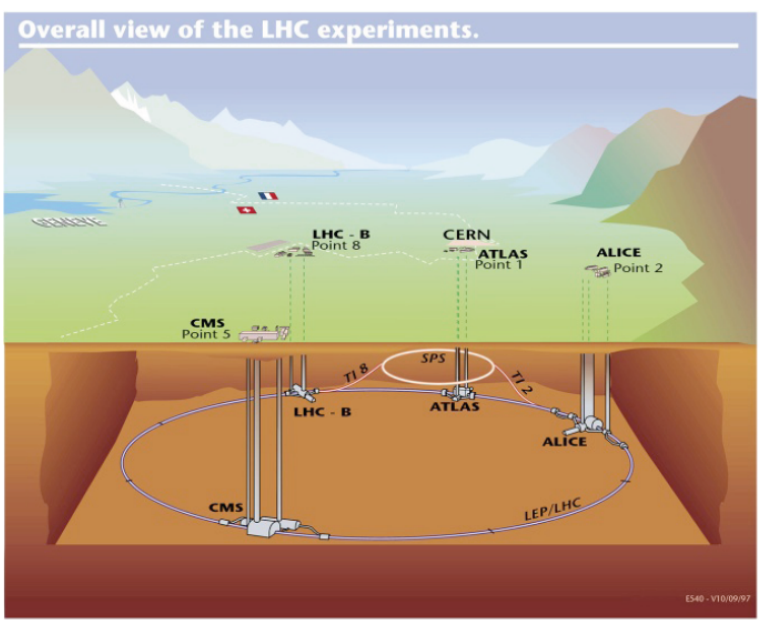

Figure 3.1: The figure shows the overall view of the LHC experiments [25].

Table 3.1: The summary of LHC parameters for operation in 2011 [26].

Parameter	Value
Energy	3.5 TeV
β^* in Atlas and CMS	1.5 m
Bunch spacing	75 ns (50 ns)
Bunch intensity	1.2×10^{11}
Stored beam energy	63 MJ (93 MJ)
Emittance [mm.mrad]	~ 2.5
Days at peak luminosity	~ 135

3.2 Compact Muon Solenoid (CMS)

CMS at the LHC is located at Point 5 which is near the French village of Cessy and installed about 100 m underground. The CMS is 21.6 m in length, 14.6 m in diameter, and its total weight is 12,500 t. It is characterized by a high magnetic field configuration for the precise momentum measurement of muon and high energy charged particles and good electromagnetic energy resolution with wide geometric coverage and efficient lepton identification.

Figure 3.2 shows an overall layout of the CMS detector. A 3.8 T superconducting solenoid surrounds the Silicon Pixel and Strip Tracker, the Electromagnetic Calorimeter (ECAL) and the Hadron Calorimeter (HCAL). Muon system is installed outside of the superconducting solenoid and inside the return yoke of the magnet.

CMS adopts the coordinate system that the origin is located at the nominal collision point in the center of the detector. The x-axis is pointing toward the center of the LHC, and the y-axis is pointing upward, and the z-axis points along the beam direction from Point 5 to the Jura Mountains. The azimuthal angle ϕ is measured in the $x-y$ plane, the polar angle θ is measured from the z-axis, and pseudorapidity (η) is defined as - ln $\tan(\theta/2)$. The transverse momentum (p_{T}) and transverse energy (E_{T}) are measured from the x and y components, and the missing-transverse-energy (E_{T}^{miss} or MET) is measured by the imbalance of energy in the $x-y$ plane.

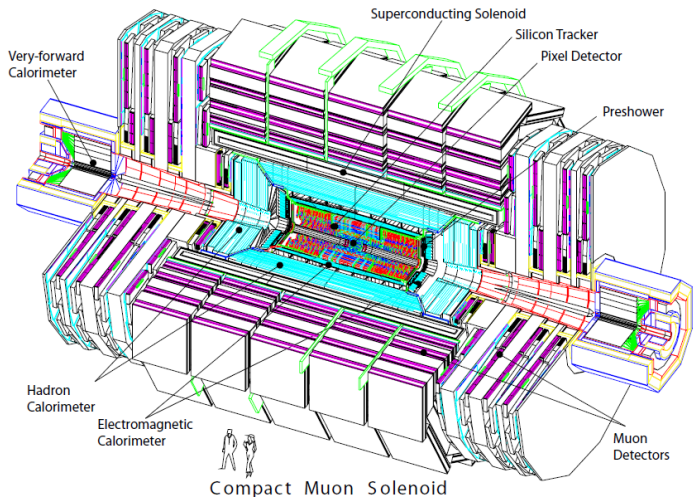

Figure 3.2: The overall layout of the CMS detector.

3.2.1 The Superconducting Magnet

The superconducting magnet [27, 28] in CMS is designed to achieve a high magnetic field up to 4 T in a free bore of 6 m diameter and 12.5 m length while a stored energy reaches 2.6 GJ at full current. The flux returns through a 10,000 t yoke composed of 11 large elements, 5 barrel wheels and 6 endcap disks including the coil and its cryostat. The return field is large enough to saturate 1.5 m of iron yoke. The cold mass is reinforced NbTi conductor in 4-layer winding and at a weight of 220 t. The superconducting solenoid provides a large bending power (12 Tm) and it allows the muon system to have full geometric coverage.

3.2.2 The Inner Tracker

The inner tracker [29, 30] in CMS is designed to perform a precise and efficient measurement of the trajectories of charged particles and secondary vertices. It has a length of 5.8 m and a diameter of 2.5 m. The tracking system with coverage up to $|\eta| < 2.5$ consists of a pixel tracker and a silicon strip tracker. Figure 3.3 shows overview of the tracker layout.

The pixel is composed of three cylindrical barrel layers at radii of 4.4 cm, 7.3 cm and 10.2 cm and surrounds the interaction point. To enhance precision, two disks of pixel modules are located on each side. In total, the pixel tracker covers an area of about 1 m^2

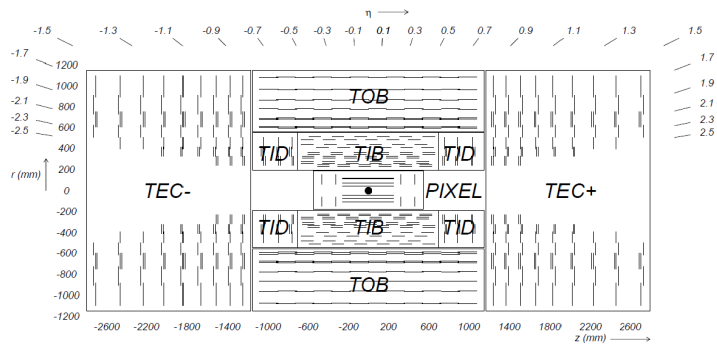

Figure 3.3: The overview of the tracker layout.

with 66 million pixels.

The silicon strip tracker is installed in the radial region between 20 cm and 116 cm. The silicon tracker consists of the Tracker Inner Barrel and Disks (TIB/TID), the Tracker Outer Barrel (TOB), and the Tracker EndCaps (TEC+ and TEC-). The TIB/TID with 4 barrel layers and 3 disks extended in radius towards 55 cm is surrounded by the 6 layers of TOB which has an outer radius of 116 cm and $|z| < 118$ cm. Each TEC is composed of 9 disks and covers the region of 124 cm $< |z| <$ 282 cm and 22.5 cm $< |r| <$ 113.5 cm. In total the silicon strip tracker has 9.3 million strips and 198 m^2 of active silicon area, and it is the largest silicon tracker ever built.

3.2.3 The Electromagnetic Calorimeter (ECAL)

The Electromagnetic Calorimeter (ECAL) [31, 32, 33] with coverage up to $|\eta| < 3$ is made of lead tungstate ($PbWO_4$) crystals and has three subsystems, the barrel ECAL (EB), endcaps (EE), and the Preshower. In order to detect the scintillation light, Avalanche Photodiodes (APDs) are installed in the barrel, and Vacuum Phototriodes (VPTs) are in the endcap region. The layout of the ECAL calorimeter is shown in Figure 3.4.

The EB covers the pseudorapidity range of $|\eta| < 1.479$, and composed of 61,200 crystals. The tapered crystals are mounted with a small angle (3°) with respect to the vector from the nominal interaction vertex to avoid cracks aligned with particle trajectories. The EB crystal cross-section is about 0.0174 $\times$ 0.0174 in η-ϕ, and it is 22 $\times$ 22 mm^2 at the

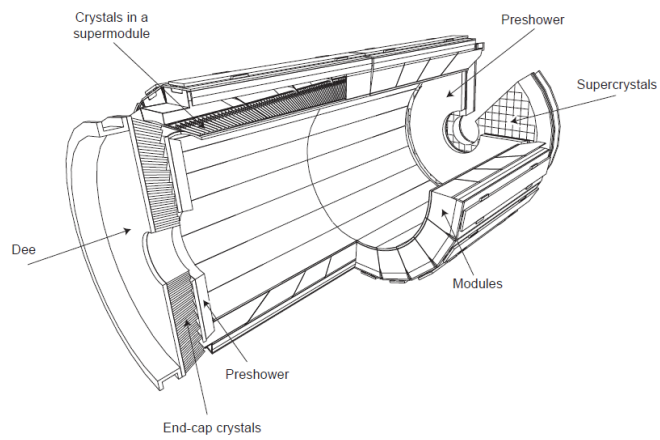

Figure 3.4: The isometric view of the ECAL calorimeter.

front face and 26 $\times$ 26 mm^2 at the rear. The crystal length of 230 mm corresponds to radiation lengths of 25.8 X_0. In total the EB has a volume of 8.14 m^3 and a weight of 67.4t.

The EE with coverage of $1.479 < |\eta| < 3.0$ consists of supercrystals (SCs) which are grouped by 5 $\times$ 5 crystals. In total, the EE has 138 standard SCs and 18 special partial supercrystals. The EE is divided into 2 halves named Dees, and each Dee has 3,662 crystals. The EE crystal cross section is 28.62 $\times$ 28.62 mm^2 at the front and 30 $\times$ 30 mm^2 at the rear. The crystals are 220 mm in length, corresponding to 24.7 X_0 radiation lengths. The EE is by volume of 2.90 m^3 and weights 24.0 t.

The preshower is designed to reject neutral pion and identify electrons against other ionizing particles and to improve the position measurement of electrons and photons. The preshower placed in front of the endcaps crystals covers a region of $1.653 < |\eta| < 2.6$. The preshower, a sampling calorimeter, consists of two layers of lead radiators and silicon strip sensors. The lead radiators initiate electromagnetic showers from incoming photons or electrons, and the silicon strip sensors measure the deposited energy and the transverse shower profiles. The total thickness of the preshower is 20 cm. The first sensor plane is installed at radiation lengths of 2 X_0, and the second plane is at an additional 1 X_0 from the first. Thus about 95 % of photon shower starts before the second sensor plane.

The energy resolution of the ECAL can be parameterized as following [24].

$$(\frac{\sigma}{E})^2 = (\frac{S}{\sqrt{E}})^2 + (\frac{N}{E})^2 + C^2 \tag{3.1}$$

Where S is the stochastic term, N the noise term, and C the constant term. A typical energy resolution was found to be S = 2.8 %, N = 0.12, and C = 0.30%, but the beam-test taken 2006 achieves a 10 % improvement of the noise performance.

3.2.4 The Hadron Calorimeter (HCAL)

The Hadron Calorimeter (HCAL) [24, 34, 35, 36, 37, 38] consists of the Hadron Barrel (HB), the Hadron Endcap (HE), the Hadron Outer (HO) and the Hadron Forward (HF) calorimeters. The layout of the HCAL calorimeter is shown in Figure 3.5.

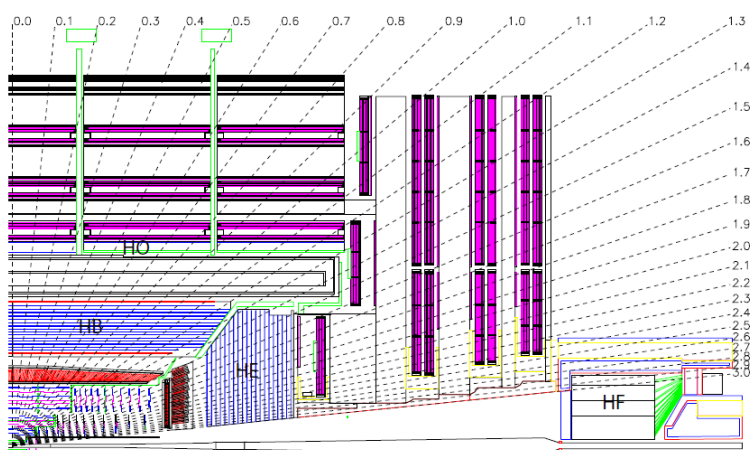

Figure 3.5: The schematic view of HCAL calorimeter.

A brass/scintillator sampling HB and HE surround the ECAL and covers the pseudorapidity range of $|\eta| < 3$. The HB is covers a range of $|\eta| < 1.3$, and the HE has coverage of $1.3 < |\eta| < 3$. The HB and HE are constructed by flat brass absorber plates, and the absorber is designed to minimize the cracks between HB and HE. Wavelength-shifting (WLS) fibers are embedded in the scintillator tiles in order to convert the scintillation light, and this light is detected by Hybrid photodiodes (HPDs). The HO is installed to improve shower

sampling with about 11 hadronic interaction lengths in front of it. A segmentation ($\Delta\eta$, $\Delta\phi$) is (0.087, 0.087).

In forward region an iron/quartz-fiber HF calorimeter extends coverage up to a pseudo-rapidity range of $|\eta| < 5$, and photomultipliers detects the Cherenkov light emitted in the quartz fibers. The HF calorimeter consists of a cylindrical steel absorber structure with an outer radius of 130.0 cm. The front face of the calorimeter is located at 11.2 m from the interaction point. The structure is azimuthally subdivided into 20° modular wedges, and total 36 wedges are divided into two sides of HF+ and HF-. Figure 3.6 shows transverse segmentation of the HF towers, and each tower corresponds to 0.175 $\times$ 0.175 ($\Delta\eta \times \Delta\phi$) with the exception of the two inner η rings that are twice as wide in ϕ direction.

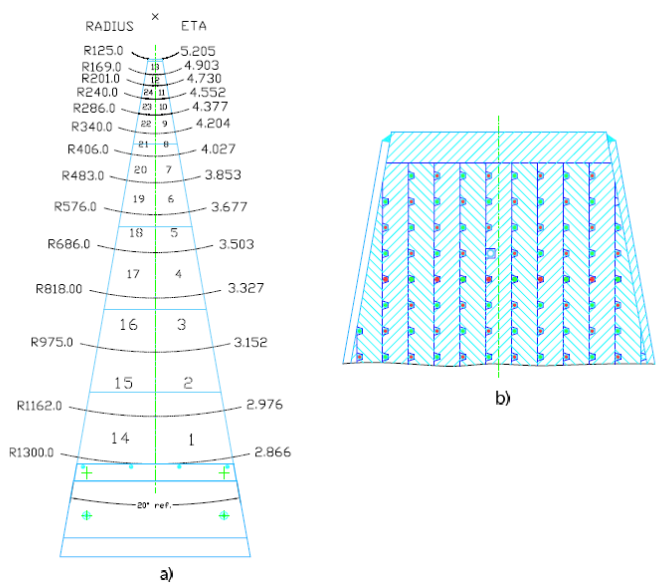

Figure 3.6: a) Transverse segmentation of the HF towers are shown. b) An expanded view of the wedge is illustrated [38].

A cross sectional view of the HF is shown in Figure 3.7. A steel absorber consists of 5 mm thick grooved plates, and fibers are inserted in these grooves. The fibers run parallel to the beam line. The detector is divided into two effective longitudinal segments, long and short fibers. The long fibers run over the full depth of the absorber (165 cm $\sim$ 10 λ_I), and the short fibers start at a depth of 22 cm in front of the detector. Long and short fibers

alternate in these grooves, and these two sets of fibers are read out separately.

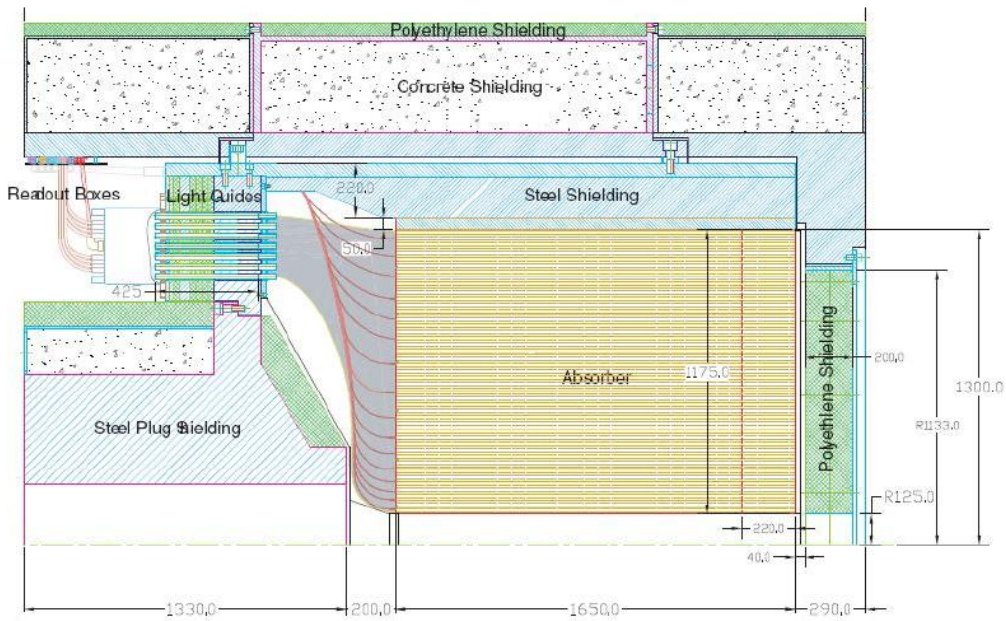

Figure 3.7: The cross sectional view of the HF.

This arrangement is in order to distinguish showers generated by electrons and photons, which deposit a large fraction of their energy in the first 22 cm, from those generated by hadrons, which produce nearly equal signals in both calorimeter segments on average. The long fiber is referred as L and the short fiber is S.

3.2.5 The Muon System

The muon system [24, 39, 40] consists of three types of gaseous particle detectors for identifying muon. The aluminium Drift Tubes (DT) is installed in the barrel region, the Cathode Strip Chambers (CSC) is in the endcap region, and the Resistive Plate Chambers (RPC) is used in order to improve the muon system performance.

The DT with coverage of $|\eta| < 1.2$ is installed inside the iron yoke and is composed of four stations which are concentric cylinders around the beam line. The first three inner cylinders contain 8 chambers with 2 groups of 4 and 4 chambers. The 8 chambers measure the muon coordinate in the $r-\phi$ bending plane, and the 4 chambers perform a measurement

in the z direction. The fourth station has 2 sets of 4 chambers, and they provide the best angular resolution.

The CSC is installed in $0.9 < |\eta| < 2.4$ where the particle rates are high and high magnetic field is large. The CSC is designed to have fast response, fine segmentation, and the radiation resistance in order to identify muon fast and effectively. The CSC consists of 4 stations which are installed perpendicular to the beam line. The cathode strips of each chamber provide a precision measurement in the $r-\phi$ bending plane, and the anode wires measure η and the beam-crossing time of muon.

The RPCs with 6 layers are embedded in the barrel muon system. The first two stations each have two layers, and the last one station has one. In the endcap region, the RPC plane is installed in each of the first three stations. The RPCs is designed for the trigger (even for low-p_{T} track), improvement of the time resolution for bunch-crossing identification, and a good p_{T} resolution.

Chapter 4

Data Set and Event Selection

A central electron is reconstructed by the inner tracker and ECAL, and a forward electron is reconstructed by the forward calorimeter (HF). We use muons reconstructed by tracker and muon system. We adopt CMS selection criteria for selecting electrons and muons. We also demand the opposite-signed dilepton.

4.1 Data Set

This analysis makes use of 2.2 fb^{-1} of proton-proton collision data collected in 2011 by CMS detector at the LHC with a center-of-mass energy of 7 TeV. Table 4.1 summarizes the data sets, and Table 4.2 gives details on the Monte Carlo signal and background samples. The $t\bar{t}$, $Z \to \tau\tau$, diboson (WW, WZ, ZZ), W inclusive, and QCD decays are considered backgrounds. Signal $Z/\gamma^* \to ee$ and $Z/\gamma^* \to \mu\mu$ and background $Z/\gamma^* \to \tau\tau$ are simulated through a Next-to-Leading Order (NLO) calculation using the POWHEG generator [41, 42, 43], and PYTHIA [44] is used for parton showering with the NLO Parton Distribution Functions (PDFs) of CT10 [45]. Background sample of $t\bar{t}$ is generated using MadGraph [46] and PYTHIA, and W inclusive is processed by MadGraph and TAUOLA [47]. PYTHIA is used for diboson (WW, WZ, ZZ) and QCD. All generated events are processed through the CMS detector simulation [48, 49], and finally the simulated events are reconstructed by CMSSW4_2_X.

Table 4.1: All data were collected in 2011 at $\sqrt{s} = 7$ TeV and amounts to 2.2 fb^{-1}.

Channel	Run-range	Data set	Integrated Luminosity [pb^{-1}]
Electron	160404-163869	/DoubleElectron/Run2011A-May10ReReco-v1	215
	165088-167913	/DoubleElectron/Run2011A-PromptReco-v4	930
	170722-172619	/DoubleElectron/Run2011A-05Aug2011-v1	371
	172620-173692	/DoubleElectron/Run2011A-PromptReco-v6	663
Muon	160404-163869	/DoubleMu/Run2011A-May10ReReco-v1	215
	165088-167913	/DoubleMu/Run2011A-PromptReco-v4	930
	170722-172619	/DoubleMu/Run2011A-05Aug2011-v1	371
	172620-173692	/DoubleMu/Run2011A-PromptReco-v6	663

Table 4.2: Monte Carlo signal and background samples are listed with integrated luminosity in pb^{-1}.

Monte Carlo sample	Cross Section [pb]	Integrated Luminosity [pb^{-1}]
DYToEE_M-20_CT10_TuneZ2_7TeV-powheg-pythia	1666.0	18000
DYToMuMu_M-20_CT10_TuneZ2_7TeV-powheg-pythia	1666.0	18000
TT_TuneZ2_7TeV-pythia6-tauola	157.5	6918
DYToTauTau_M-20_CT10_TuneZ2_7TeV-powheg-pythia-tauola	1666.0	11967
WJetsToLNu_TuneZ2_TeV-madgraph-tauola	32206.0	4407
WW_TuneZ2_7TeV_pythia6_tauola	27.8	151848
WZ_TuneZ2_7TeV_pythia6_tauola	10.5	407378
ZZ_TuneZ2_7TeV_pythia6_tauola	4.3	976880
QCD_Pt-20to30_EMEnriched_TuneZ2_7TeV-pythia6	236100000.0	14.2
QCD_Pt-30to80_EMEnriched_TuneZ2_7TeV-pythia6	59440000.0	19.3
QCD_Pt-80to170_EMEnriched_TuneZ2_7TeV-pythia6	898200.0	57.0

4.2 Electron Selection

4.2.1 Electron Selection in Central Region

ECAL gives good mass resolution ($\sim$ 1% at 100 GeV) and the tracker performs efficient and precise measurement. We use the Gaussian Sum Filter (GSF) [50, 51] algorithm for electron which is identified by fitting seeds in the ECAL superclusters and tracker. An electron or a positron is reconstructed within $|\eta| <$2.5 excluding a small region 1.4442 $< |\eta| <$1.560.

Good electron candidates are defined by Working Point 80 (WP80) selection crite-

ria [52] as illustrated in Table 4.3. This selection rejects to select electrons from photon conversions as well as discriminating electrons from jets and photon. The jet-like electrons are filtered by track-based and calorimetry-based isolation criteria and the ratio of hadronic to electromagnetic energy (H/E). Photon rejection is based on track information. Electrons from photon conversions are effectively removed by requiring no missing hits in the inner pixel and more than 0.02 in separate distance and $\Delta\cot\theta$ of the partner tracks.

Table 4.3: WP80 selection criteria. Note that the ECAL energy corrections are not applied to the E_{T} and H/E ratio used in this analysis*.

Selection variable	EB	EE
Track isolation in $dR = 0.3$ / electron E_{T}^{*}	<0.09	<0.04
ECAL isolation in $dR = 0.3$ / electron E_{T}^{*}	<0.07	<0.05
HCAL isolation in $dR = 0.3$ / electron E_{T}^{*}	<0.10	<0.025
$\sigma_{i\eta,i\eta}$	<0.01	<0.03
$\lvert\Delta\phi\rvert$	<0.06	<0.03
$\lvert\Delta\eta\rvert$	<0.004	<0.007
H/E*	<0.04	<0.025
Missing hits in inner pixel	=0	=0
Distance of the partner track	> 0.02	> 0.02
$\Delta\cot\theta$ of the partner track	> 0.02	> 0.02

4.2.2 Electron Selection in Forward Region

The A_{FB} measurement suffers dilution due to the unknown quark direction. However, the CMS experiment improves the measurement using electrons up to $|\eta| < 5$. Since a quark direction ambiguity is highly reduced in a large rapidity region, the A_{FB} measurement in CMS results in a less diluted measurement.

An electron, directed forward region of $|\eta| >3$, is reconstructed by the forward calorimeter that is originally optimized for jet detection. The forward calorimeter reconstruction is performed by using long and short fiber information, which are alternately embedded and separately read out in each tower. In order to distinguish electron/photon showers from hadron showers, the short fibers are embedded at a depth of 22 cm from the front of the

detector, but the long fibers are installed to the full depth of 165 cm. Since electromagnetic shower deposits most of the energy in the first 22 cm, the electron is identified by long fibers (see Figure 4.1 and 4.2).

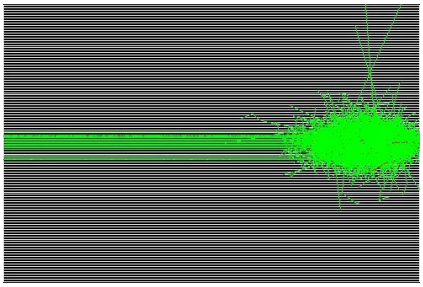

Figure 4.1: A typical electron (100 GeV) shower in the forward calorimeter (by Nural Akchurin and Ken Carrell).

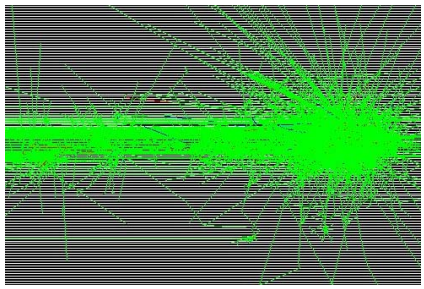

Figure 4.2: A typical proton (100 GeV) shower in the forward calorimeter (by Nural Akchurin and Ken Carrell).

The electron reconstructed by the energy sum of L in (3×3) HF towers is selected based on transverse and longitudinal shower shapes. Since the hadron shower shape is broader than the electron shower, the hadron-like object is filtered by the ratio of the energy sum of L in 3×3 ($L9$) to energy sum of L in 5×5 ($L25$). Also, the combination of L of the core tower, (3×3) S and (3×3) L is used for selecting good electron candidates in the forward region. The selection criteria are [53]:

1. $L9/L25 > 0.96$,
2. $L1/L9 - 1.125 \times (S9/L9) > 0.4$

4.3 Muon Selection

The CMS experiment enjoys excellent muon identification and momentum resolution, good dimuon mass resolution ($\sim 1\%$ at 100 GeV), and unambiguous muon charge determination. Since the lepton charge and dilepton mass are one of the main ingredients in the A_{FB} measurement, CMS is well suited for this analysis.

A muon is reconstructed based on hits in the tracker and the muon system. If a muon identified by hits in the muon detector, it is referred to as Stand-alone muon. If reconstruc-

tion of muon starts with tracks in inner tracker and matches them with muon system, it is labeled as Tracker muon. A muon is called as Global muon in case a muon algorithm starts with the muon segment and then finds for hits in tracker [39].

In this analysis, muons tagged as both Tracker and Global are considered to be good muon candidates. Also, $|\eta|$ <2.1 and $P_{\mathrm{T}} > 20$ GeV$/c$ are required for these muons. In addition, muons are selected based on the standard CMS muon identification requirements summarized in Table 4.4. The track-based isolation can remove fake muon, and signal muon can be selected using impact parameter $dxy < 2$ mm with respect to the beam spot. The filtered muon based on the number of hits on tracker and muon system and normalized χ^2 of the global fit is a high-quality muon candidate.

Table 4.4: Muon selection criteria [13].

Selection variable	
Track isolation in $dR = 0.3$	< 3 GeV
Hits in the track	> 10
Hits in the pixel detector	≥ 1
Number of used muon stations	> 1
Hits in the Muon system	≥ 1
Impact parameter, dxy	< 2 mm
Normalized χ^2 for the global fit	<10

Since muon detection is based on hits in tracker and muon system, the alignment of these system is an important requirement. We examine the mis-alignment effect on the A_{FB} measurement. Detailed discussion is in Chapter 8.

4.4 Lepton Pair Selection

The A_{FB} measurement requires opposite-signed dielectron and dimuon events. The forward electron $|\eta| > 3$ charge is unknown because the tracker coverage does not extend to forward region. We select a central electron and a forward electron for the A_{FB} measurement. The electron and positron are determined based on the central electron charge in order to

determine $\cos\theta^*$. To suppress background events, we select events that both a central electron and a forward electron decay to same z-direction because pair of a central electron and a forward electron are most likely from a boosted Z in high η.

Now that event selection has been completed, and we are approximately left with 6 million MC pairs and 0.8 million data pairs for central dimuons, 4 million MC pairs and 0.5 million data pairs for central dielectrons, and 0.4 million MC pairs and 45 thousand data pairs for central-forward electrons. Next, lepton corrections are applied to the MC and the data samples.

Chapter 5

Corrections

The target of this analysis is to measure the A_{FB} as a function of dilepton invariant mass and to unfold the measured A_{FB} to the *true* A_{FB} aided by MC. We applied an energy scale and resolution, pile-up, and detection efficiency corrections. The correction factors are examined within the Z boson mass window.

5.1 Energy Scale and Resolution

One of the critical steps in the A_{FB} measurement is the precise measurement of the single lepton transverse energy and dilepton invariant mass. In order to ensure a high level precision, an adequate detector calibration is necessary for energy and momentum measurements. We select a good electron and muon by the selection criteria listed in Tables 4.3 and 4.4. Also, Z boson mass window, $75 < M_{l^+l^-} < 108$ GeV/c^2 is used in order to suppress background events.

5.1.1 Electron in Central Region

Figure 5.1 shows electron transverse energy in 10 η bins. The η bin edges are -2.5, -2.0, -1.5, -1.0, -0.5, 0.0, 0.5, 1.0, 1.5, 2.0, 2.5. In Figure 5.1, the data and MC events show different behavior in $1.0 < |\eta| < 2.5$. Also, the peaks of dielectron invariant mass in data and MC are clearly separated and the mass resolution in data is broader than that of MC's, as shown in Figure 5.3. Furthermore, the ratio of data to MC distribution is varying from 0.8 to 1.4, and it is not negligible. As a result, we apply electron energy scale and smearing

corrections to data and MC samples.

As shown in Table 4.1, 2011 data are divided into four sets, named as May10, Prompt4, Aug5, and Prompt6. Updated calibration is applied for the run range of 160404 to 163869 and 170722 to 172619, and they are re-reconstructed and re-named as May10 and Aug5. According to Figure 5.5, the invariant mass distributions of dielectron, before the energy scale and resolution correction, the prompt data sets show a significant difference between the data and MC while the re-reconstructed data sets (May10 and Aug5) show acceptable agreements. This means that global correction factors over all runs cannot be used.

Thus, the energy scale factors are estimated in individual data sets with respect to 10 η values between -2.5 and 2.5 in order to obtain an optimized energy scale correction. The energy scale factors in each η bin are tested by a χ^2 method between the data and MC in the range of 75$< M_{e^+e^-} <$108 GeV/c^2. The energy scale factor is determined where the energy scale factor minimize the χ^2, and its error is defined by allowing the χ^2 to increase by 1.

The energy smearing factors tune MC as to have the same mass resolution as in data. After the energy scale factors are applied to data, the energy smearing factors for MC are found using the same χ^2 test method as the energy scale factors. In order to get stable and accurate energy scale and resolution factors, χ^2 test process are iterated three times. The maximum energy scale factor is about 1.05 for data, and the maximum energy smearing factor for MC is about 0.04. The energy scale factors for data are listed in Table 5.1, and the energy smearing factors for MC are in Table 5.2. After applying in those factors into data and MC, individual data sets show good agreements (see Figure 5.6).

5.1.2 Electron in Forward Region

Figure 5.7 shows the dielectron invariant mass of a central and a forward electron before the forward electron energy scale and resolution corrections. The shift is about 5 GeV$/c^2$, requiring the energy scale and resolution corrections for the forward electron.

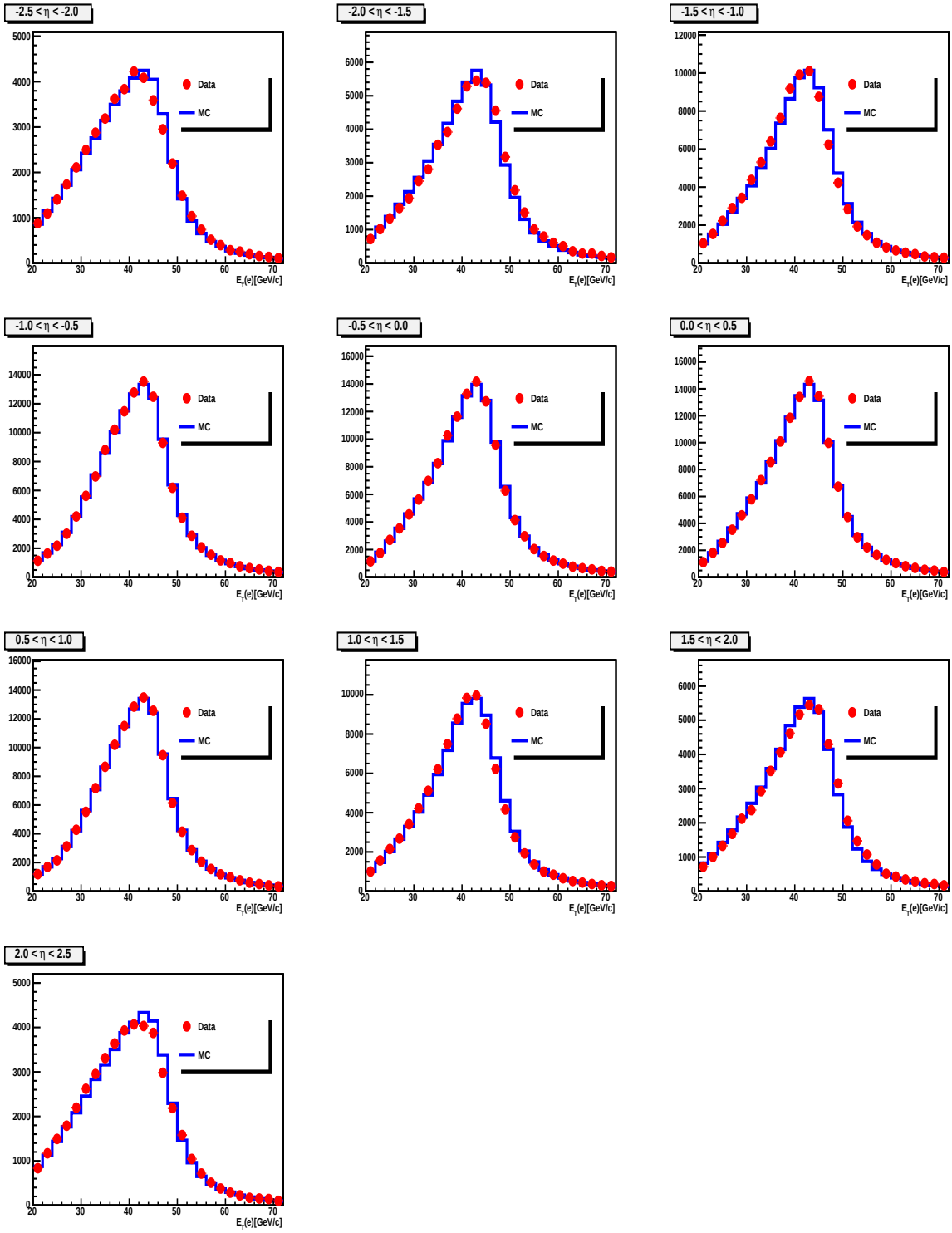

Figure 5.1: Transverse energy of electron with respect to 10 different η bins in data and MC.

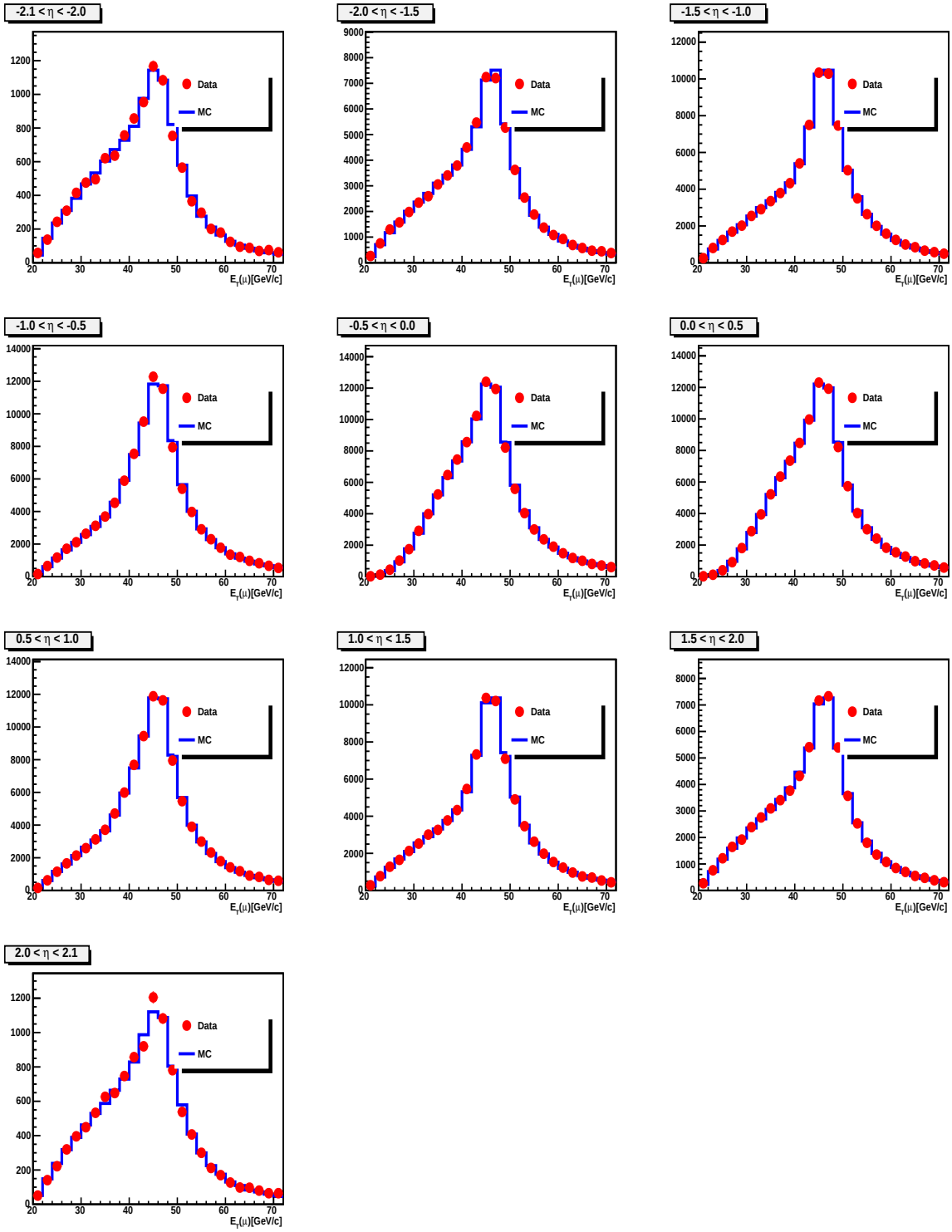

Figure 5.2: Transverse energy of muon in 10 η bins.

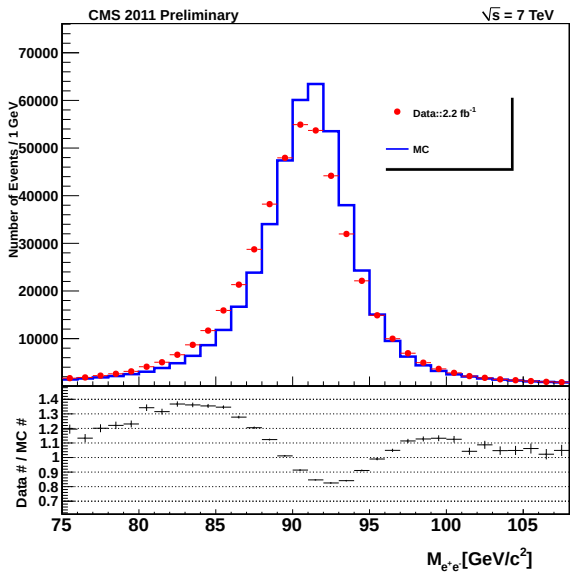

Figure 5.3: The invariant mass of dielectron (top) and the ratio between data and MC varies from 0.8 to 1.4 (bottom).

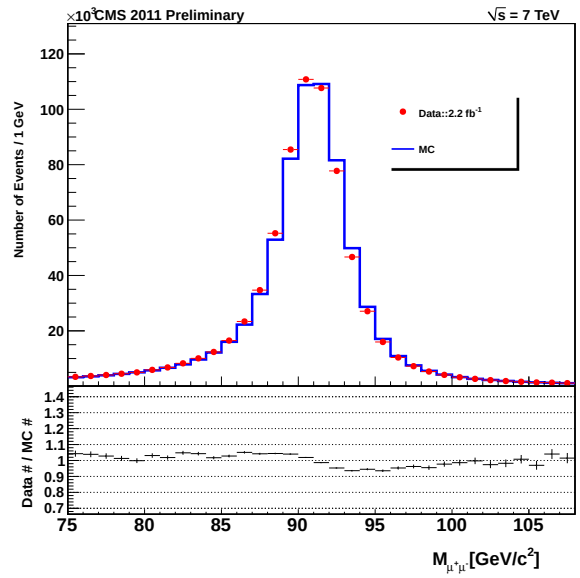

Figure 5.4: The invariant mass dimuons (top) and the ratio between data and MC varies from 0.9 to 1.1 (bottom).

In order to calculate these factors, we take account of 18 towers in HF+ and HF- and test them using the same correction method as for the central electron. The HF $|\eta|$ edges are 2.964, 3.139, 3.314, 3.489, 3.664, 3.839, 4.013, 4.191, 4.363, 4.538 in both HF- and HF+. The forward electron energy is scaled by 1.066 to 1.221, and the energy smearing by a factor of 0.088 to 0.177. These factors are listed in Table 5.3 and shown in Figure 5.8.

5.1.3 Muons

In Figure 5.4, the data and MC distributions are in good agreement. In order to further examine the small difference, we show the ratio of data to MC in the bottom of Figure 5.4. The distribution shift is 7-8 times less than that of the electron channel. Moreover, we do not see a significant difference in the transverse energy distribution in data and MC samples (see Figure 5.2). We take into account of uncertainties in energy scale and resolution as a part of systematic uncertainty.

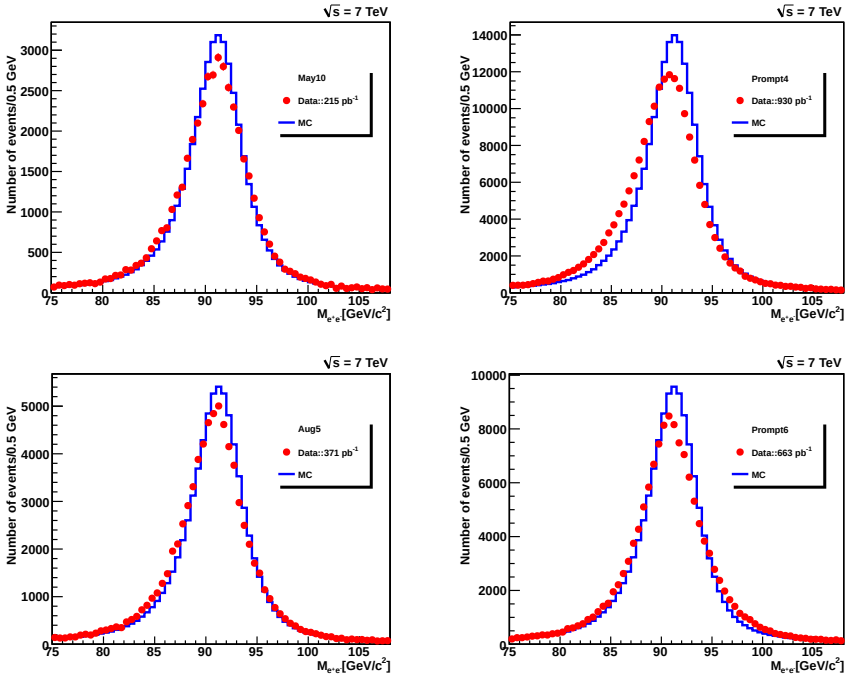

Figure 5.5: The dielectron invariant mass comparison between data and MC before the energy scale and resolution correction applied.

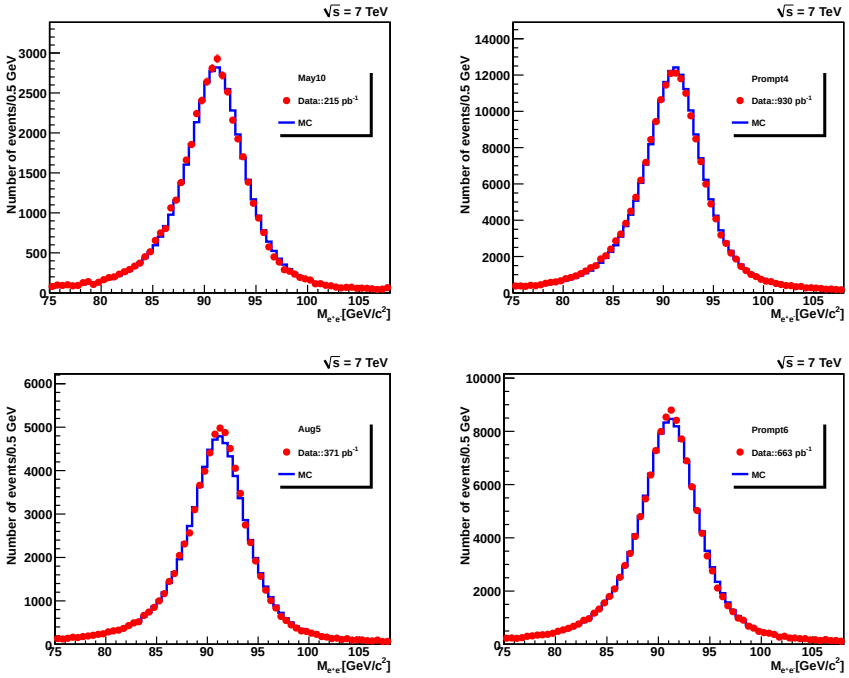

Figure 5.6: The invariant mass of dielectron in data and MC is corrected by energy scale and resolution correction factors. The maximum energy scale factor is about 1.05 for data, and the maximum energy smearing factor for MC is about 0.04.

Table 5.1: The ECAL energy scale factors applied in data in the electron channel.

Eta	May10	Prompt4	Aug5	Prompt6
$-2.5< \eta < -2.0$	1.0117 ± 0.0009	1.0474 ± 0.0007	0.9937 ± 0.0007	0.9713 ± 0.0007
$-2.0< \eta < -1.5$	0.9941 ± 0.0010	1.0018 ± 0.0010	0.9951 ± 0.0020	0.9785 ± 0.0007
$-1.5< \eta < -1.0$	1.0063 ± 0.0010	1.0100 ± 0.0006	1.0142 ± 0.0006	1.0181 ± 0.0007
$-1.0< \eta < -0.5$	0.9976 ± 0.0006	1.0007 ± 0.0005	1.0047 ± 0.0006	1.0064 ± 0.0006
$-0.5< \eta <0.0$	0.9967 ± 0.0008	1.0032 ± 0.0006	1.0014 ± 0.0005	1.0041 ± 0.0007
$0.0< \eta <0.5$	0.9962 ± 0.0009	1.0004 ± 0.0006	1.0008 ± 0.0005	1.0025 ± 0.0007
$0.5< \eta <1.0$	0.9962 ± 0.0009	0.9989 ± 0.0005	1.0023 ± 0.0005	1.0046 ± 0.0005
$1.0< \eta <1.5$	1.0028 ± 0.0006	1.0109 ± 0.0008	1.0182 ± 0.0009	1.0167 ± 0.0010
$1.5< \eta <2.0$	0.9950 ± 0.0008	1.0036 ± 0.0010	0.9879 ± 0.0005	0.9751 ± 0.0009
$2.0< \eta <2.5$	1.0126 ± 0.0009	1.0597 ± 0.0009	0.9884 ± 0.0005	0.9659 ± 0.0007

Table 5.2: The ECAL energy smearing factors applied in MC in the electron channel.

Eta	energy resolution factors
$-2.5< \eta < -2.0$	0.041 ± 0.002
$-2.0< \eta < -1.5$	0.035 ± 0.003
$-1.5< \eta < -1.0$	0.023 ± 0.002
$-1.0< \eta < -0.5$	0.011 ± 0.002
$-0.5< \eta <0.0$	0.010 ± 0.002
$0.0< \eta <0.5$	0.011 ± 0.002
$0.5< \eta <1.0$	0.013 ± 0.002
$1.0< \eta <1.5$	0.020 ± 0.003
$1.5< \eta <2.0$	0.028 ± 0.005
$2.0< \eta <2.5$	0.040 ± 0.002

5.2 Pile-up

As the instantaneous luminosity increases, multiple interactions occur much more frequently and introduce so-called pile-up [54]. Since the multiple interactions are reflected in the number of vertices, we use the number of vertices averaged over all runs in order to investigate the uncertainties introduced by phenomenon.

Figures 5.9 and 5.10 show distributions of the number of vertices averaged over all runs for the central electron and muon channels. Due to the significantly different distributions

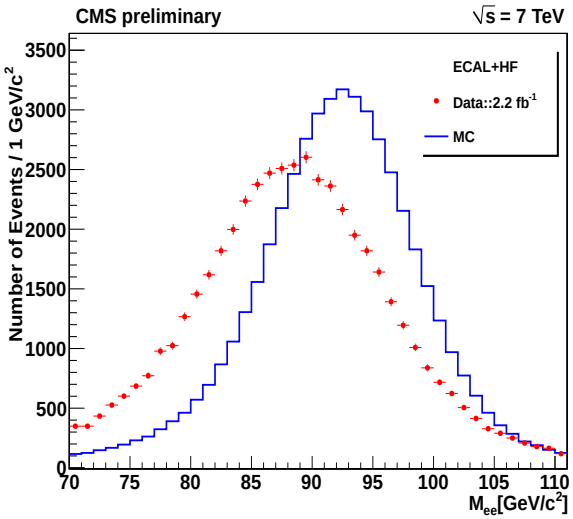

Figure 5.7: The invariant mass distribution of dielectrons is shown without the energy scale and resolution corrections. The peak of invariant mass in data is about 5 GeV$/c^2$ off from that of simulation.

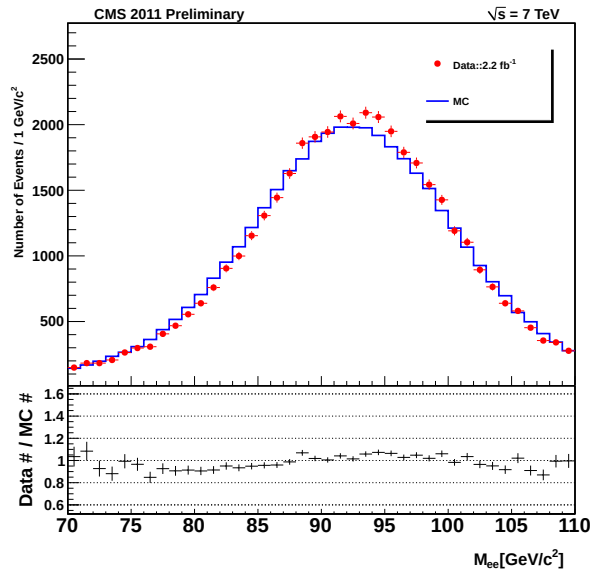

Figure 5.8: The invariant mass distribution of dielectrons with energy scale and resolution corrections. The bottom plot shows the ratio of data to MC, displaying the level of tuning between the two.

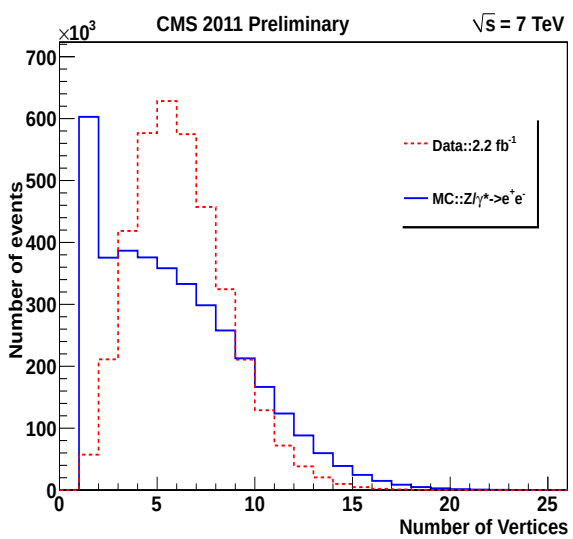

Figure 5.9: The number of vertices of the electron channel.

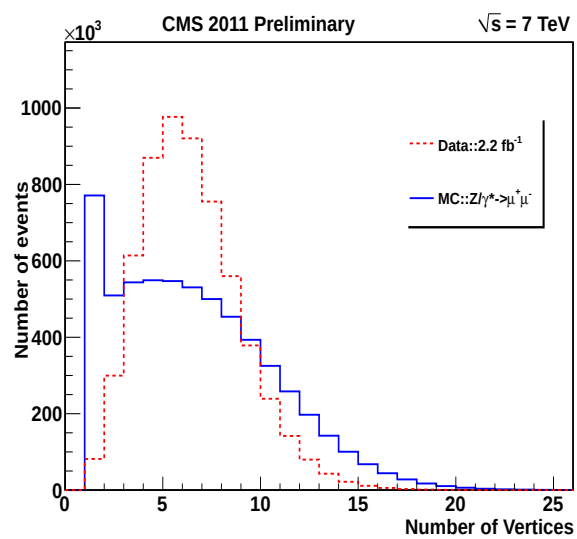

Figure 5.10: The number of vertices of the muon channel.

Table 5.3: The energy scale and resolution correction factors in HF+ and HF-.

Eta	Energy Scale	Energy Resolution
$-4.538 < \eta < -4.363$	1.096 ± 0.003	0.115 ± 0.030
$-4.363 < \eta < -4.191$	1.131 ± 0.004	0.102 ± 0.020
$-4.191 < \eta < -4.013$	1.110 ± 0.003	0.109 ± 0.020
$-4.013 < \eta < -3.838$	1.104 ± 0.004	0.093 ± 0.010
$-3.838 < \eta < -3.664$	1.081 ± 0.003	0.112 ± 0.010
$-3.664 < \eta < -3.489$	1.099 ± 0.004	0.107 ± 0.009
$-3.489 < \eta < -3.314$	1.098 ± 0.005	0.097 ± 0.008
$-3.314 < \eta < -3.139$	1.104 ± 0.003	0.117 ± 0.007
$-3.139 < \eta < -2.964$	1.221 ± 0.004	0.195 ± 0.020
$2.964 < \eta < 3.139$	1.195 ± 0.004	0.158 ± 0.020
$3.139 < \eta < 3.314$	1.084 ± 0.004	0.114 ± 0.007
$3.314 < \eta < 3.489$	1.066 ± 0.003	0.093 ± 0.008
$3.489 < \eta < 3.664$	1.106 ± 0.003	0.088 ± 0.009
$3.664 < \eta < 3.839$	1.059 ± 0.003	0.112 ± 0.010
$3.839 < \eta < 4.013$	1.056 ± 0.003	0.105 ± 0.010
$4.013 < \eta < 4.191$	1.037 ± 0.004	0.096 ± 0.010
$4.191 < \eta < 4.363$	1.090 ± 0.005	0.143 ± 0.030
$4.363 < \eta < 4.538$	1.109 ± 0.006	0.177 ± 0.030

of data vs. MC [55], the MC is tuned by event weighting to replicate the same distribution as in data. Table 5.4 shows the calculated weighting factors in the electron and muon channels. The background MC samples are also tuned using the same factors.

We evaluate the pile-up effect on the A_{FB} measurement. Although data and MC samples show a significant difference for dielectrons and dimuons, this is not a significant source of uncertainties in evaluating A_{FB}. The maximum A_{FB} deviation is about 0.008. The detailed discussion is in Chapter 8.

5.3 Electron and Muon Identification Efficiencies in Central Region

To compute the central electron and muon identification efficiencies, "tag and probe" methodology [56] is employed on a sample of high purity $Z \to l^+l^-$ events. A high purity is assured by a tight mass window cut near the Z boson peak and tight requirement of a tag leg in a

Table 5.4: The signal and background MCs are tuned to account for pile-up by the weighting factors.

Number of Vertices	dielectron	dimuon
1	0.094 ± 0.001	0.105 ± 0.001
2	0.562 ± 0.004	0.588 ± 0.003
3	1.083 ± 0.005	1.129 ± 0.005
4	1.535 ± 0.007	1.584 ± 0.006
5	1.754 ± 0.007	1.786 ± 0.006
6	1.729 ± 0.007	1.735 ± 0.006
7	1.533 ± 0.007	1.511 ± 0.006
8	1.261 ± 0.007	1.234 ± 0.005
9	0.991 ± 0.007	0.962 ± 0.005
10	0.776 ± 0.006	0.735 ± 0.005
11	0.583 ± 0.006	0.548 ± 0.004
12	0.433 ± 0.006	0.404 ± 0.004
>13	0.248 ± 0.004	0.205 ± 0.002

narrow invariant mass window, $75 < M_{l^+l^-} < 108$ GeV/c^2 which minimizes the background contribution. First, a qualified lepton is assigned as a "tag", satisfying the requirements in Table 4.3 for electron and Table 4.4 for muon. Then, another lepton is assigned as a "probe" when the invariant mass of the two falls in the mass window, $75 < M_{l^+l^-} < 108$ GeV/c^2. In the electron channel, the identification efficiency is defined in Gaussian Sum Filter (GSF) [50, 51] electron to be passed the Working Point 80 selection (WP80). The muon efficiency is the efficiency of Global or Track muon based on selection cuts listed in Table 4.4. Finally, the probe identification efficiency is calculated in terms of the 4 transverse momentum and 10 pseudorapidity bins. Total of 40 η-p_{T} efficiencies are listed in Tables 5.5 and 5.6.

At this stage, the lepton corrections are applied, and we treat MC and data in same manner for the rest of the A_{FB} measurement.

Table 5.5: Electron identification efficiency. The ratios of data to MC efficiency are given.

η	$20< P_T <30$ [GeV/c]	$30< P_T <40$ [GeV/c]	$40< P_T <50$ [GeV/c]	$50< P_T <1000$ [GeV/c]
$-2.5< \eta < -2.0$	0.955 ± 0.015	0.992 ± 0.011	0.993 ± 0.010	1.010 ± 0.018
$-2.0< \eta < -1.5$	0.970 ± 0.015	0.980 ± 0.009	0.996 ± 0.009	0.993 ± 0.015
$-1.5< \eta < -1.0$	0.912 ± 0.012	0.959 ± 0.007	0.978 ± 0.007	0.967 ± 0.012
$-1.0< \eta < -0.5$	0.922 ± 0.011	0.978 ± 0.006	0.981 ± 0.006	0.968 ± 0.010
$-0.5< \eta <0.0$	0.948 ± 0.011	0.981 ± 0.006	0.981 ± 0.005	0.966 ± 0.010
$0.0< \eta <0.5$	0.929 ± 0.011	0.979 ± 0.006	0.979 ± 0.005	0.965 ± 0.010
$0.5< \eta <1.0$	0.928 ± 0.011	0.977 ± 0.006	0.983 ± 0.006	0.969 ± 0.010
$1.0< \eta <1.5$	0.900 ± 0.012	0.951 ± 0.007	0.971 ± 0.007	0.967 ± 0.012
$1.5< \eta <2.0$	0.980 ± 0.015	0.987 ± 0.009	0.997 ± 0.009	1.000 ± 0.016
$2.0< \eta <2.5$	0.935 ± 0.014	0.986 ± 0.010	0.992 ± 0.010	0.995 ± 0.018

Table 5.6: Muon identification efficiency. The ratios of data to MC efficiency are given.

η	$20< P_T <30$ [GeV/c]	$30< P_T <40$ [GeV/c]	$40< P_T <50$ [GeV/c]	$50< P_T <1000$ [GeV/c]
$-2.1< \eta < -2.0$	0.992 ± 0.022	0.993 ± 0.017	0.993 ± 0.017	0.997 ± 0.030
$-2.0< \eta < -1.5$	1.010 ± 0.009	1.010 ± 0.007	1.010 ± 0.006	1.010 ± 0.012
$-1.5< \eta < -1.0$	0.986 ± 0.009	0.990 ± 0.006	0.989 ± 0.005	0.989 ± 0.009
$-1.0< \eta < -0.5$	0.995 ± 0.009	1.000 ± 0.006	1.000 ± 0.005	0.996 ± 0.009
$-0.5< \eta <0.0$	0.997 ± 0.009	1.010 ± 0.005	1.010 ± 0.005	1.000 ± 0.009
$0.0< \eta <0.5$	1.000 ± 0.009	1.010 ± 0.005	1.010 ± 0.005	1.010 ± 0.009
$0.5< \eta <1.0$	0.993 ± 0.009	0.998 ± 0.006	0.998 ± 0.005	0.996 ± 0.009
$1.0< \eta <1.5$	0.992 ± 0.009	0.997 ± 0.006	0.997 ± 0.005	0.996 ± 0.009
$1.5< \eta <2.0$	1.020 ± 0.010	1.030 ± 0.007	1.020 ± 0.006	1.020 ± 0.012
$2.0< \eta <2.1$	0.999 ± 0.022	0.996 ± 0.017	1.000 ± 0.017	1.000 ± 0.030

Chapter 6

Background

We consider $t\bar{t}$, $Z \rightarrow \tau\tau$, W inclusive, WW, WZ, ZZ and QCD as background since t, τ and W decay to electron or muon. The background is estimated from either MC or from data, as in the case of QCD.

6.1 Backgrounds in Central Region

The $t\bar{t}$, $Z \rightarrow \tau\tau$, W inclusive, and diboson (WW, WZ, and ZZ) backgrounds are estimated using the MC samples listed in Table 4.2. However, a data-driven method [57] is used to estimate the QCD background mainly due to the limited size of MC QCD sample.

In general, the QCD events are composed of jets and equally fake same-signed and opposite-signed lepton pairs, while the signal events consist of only opposite-signed lepton pairs. As seen in Figure 6.1, only data events contain the same-signed lepton pairs, not the MC. Therefore, the same-signed events in data can be referred to as QCD background. Figure 6.1, the distribution of invariant mass due to the same-signed muon pairs, helps estimate the QCD background in the muon channel.

However, the electron pairs are present in the same-signed event in both data and MC (see Figure 6.2) because of the charge mis-identification. Thus, the extra events in data compared to the MC in Figure 6.2 can be assumed to originate from QCD interactions.

To estimate the QCD contribution, we subtract MC (solid line in Figure 6.3) from data (data points in Figure 6.3), but the remaining events, represented by dots in Figure 6.3, show a bump at 91 GeV/c^2. In order to understand the bump, we examine the charge mis-

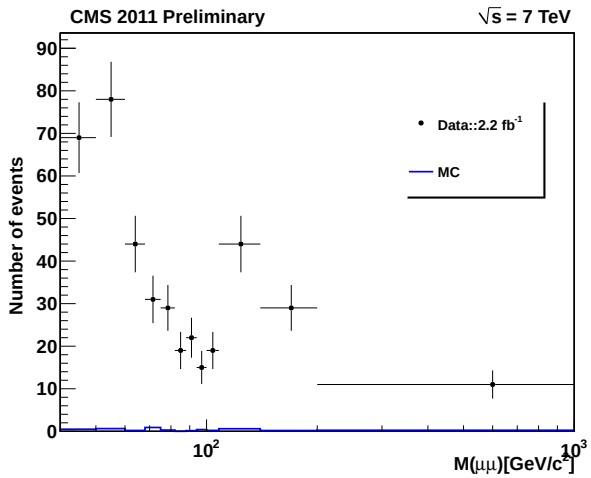

Figure 6.1: The invariant mass of same-signed dimuon event in data and signal MC.

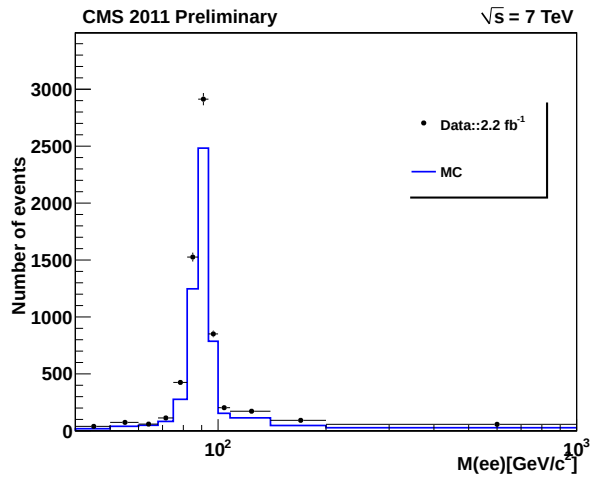

Figure 6.2: The invariant mass of same-signed dielectron event in data and signal MC.

identification rate in pairs by the ratio of same-signed events to the opposite-signed events in events that reproduce the Z mass (see Figure 6.4). The Z peak in Figure 6.3 is present because the same-signed electron pairs in data are much more numerous than in MC.

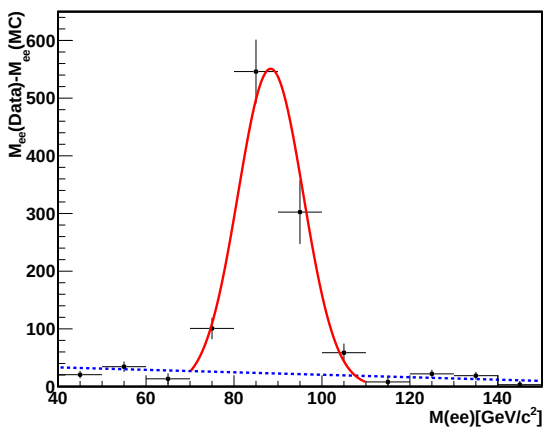

Figure 6.3: Invariant mass difference of same-signed dielectrons between data and MC.

As a result, we obtain the total number of QCD events by removing the Z-events from Figure 6.3, and each mass bin entry is determined by the MC QCD mass shapes. To gain more QCD events to get a smoother mass distribution, loose selection cut (WP95) and anti-isolation selection are used. Figures 6.7 and 6.6 shows the numbers of each of EW and QCD backgrounds in 12 mass bins in the electron and muon channels, and total background

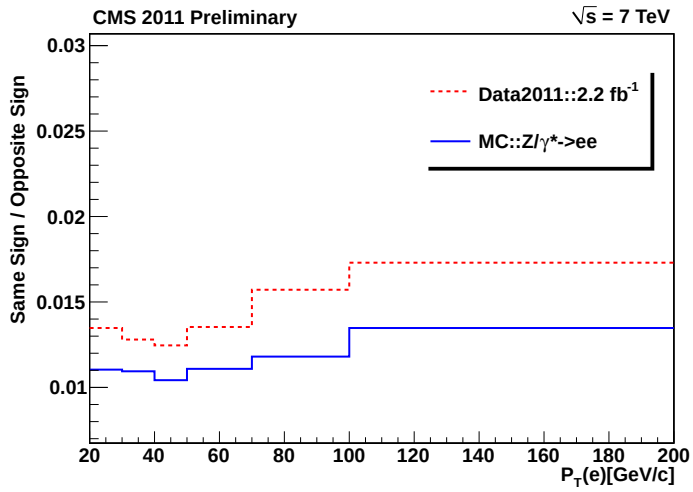

Figure 6.4: Charge mis-identification rates for electron pairs.

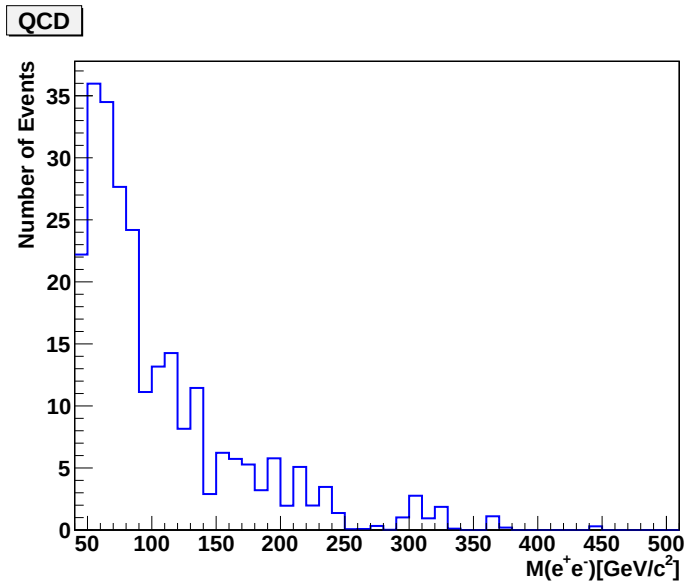

Figure 6.5: The MC QCD mass shape is shown. To increase statistics loose selection cut (WP95) and anti-isolation are used.

contribution in the electron and muon channels is listed in Table 6.1. The $t\bar{t}$ is dominant in high mass region, and $Z \rightarrow \tau\tau$ is a significant background in low mass in the central electron and muon channels.

Table 6.1: The numbers of background events in central region are estimated in 2.2 fb^{-1} of the integral luminosity.

Background	$Z \rightarrow ee$	$Z \rightarrow \mu\mu$
$t\bar{t}$	1379.9 ± 21.8	2275.0 ± 26.9
$Z \rightarrow \tau\tau$	968.1 ± 13.9	1986.0 ± 19.1
W inclusive	30.5 ± 4.0	50.2 ± 5.0
WW	194.7 ± 1.7	296.4 ± 2.0
WZ	222.9 ± 1.1	341.4 ± 1.3
ZZ	177.4 ± 0.6	281.9 ± 0.7
QCD	254.4 ± 15.9	403.0 ± 20.0

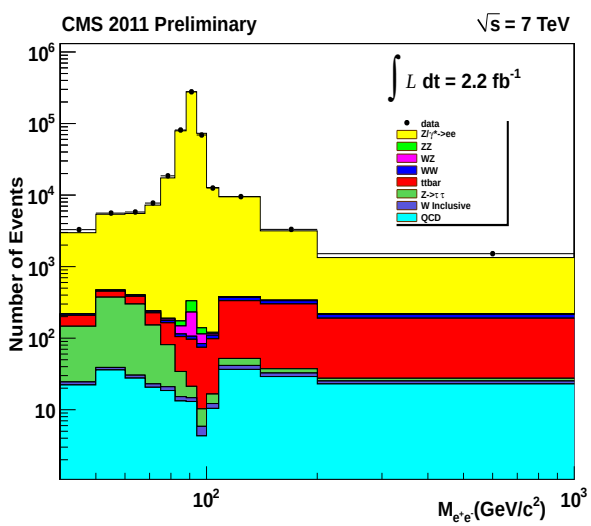

Figure 6.6: The invariant mass distribution in the electron channel.

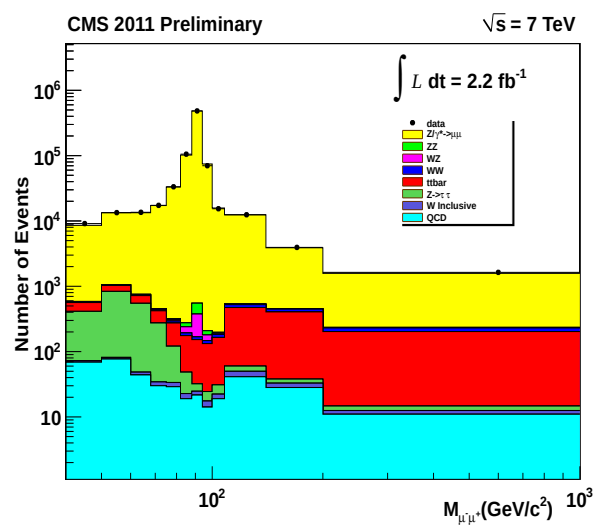

Figure 6.7: The invariant mass distribution in the muon channel.

6.2 Background in the Forward Region

Backgrounds of central and forward electron are measured based on the Monte Carlo samples shown in Table 4.2. As shown in Figure 6.8 and Table 6.2, QCD and W inclusive

events are the most dominant.

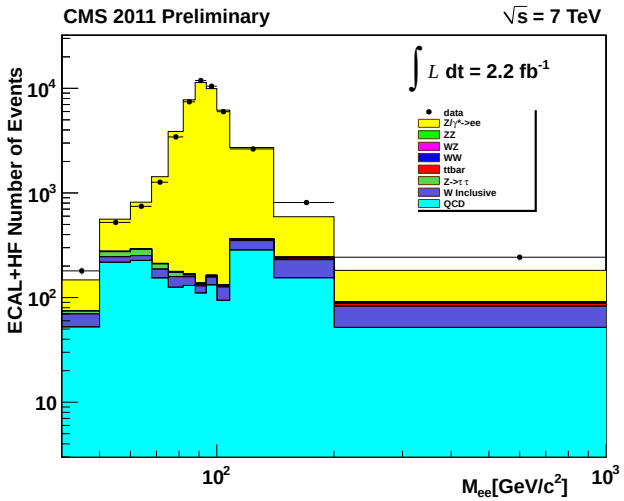

Figure 6.8: Invariant mass distributions where one electron is in the central and the second is in the forward regions.

Table 6.2: The numbers of background events are estimated in 2.2 fb^{-1} of the integral luminosity. The listed numbers of backgrounds fake the central and forward electron pairs.

Background	$Z \to ee$
$t\bar{t}$	26.8±2.6
$Z \to \tau\tau$	126.6±4.3
W inclusive	413.8±12.8
WW	13.6±0.3
WZ	13.3±0.2
ZZ	7.5±0.1
QCD	1731.6±407.1

From now on, $t\bar{t}$, $Z \to \tau\tau$, W inclusive, WW, WZ, ZZ and QCD events are estimated either by a MC or a data-driven method. The total background is less than 1 %. This is an acceptable level of combination and has no detrimental effect on the A_{FB} measurement.

Chapter 7

Results

Event selection and corrections are investigated by the distributions of transverse momentum, invariant mass, $\cos\theta^*$, and rapidity of dilepton. Then, the raw A_{FB} values are measured and unfolded in three stages: limited pre-FSR (born level before kinematic acceptance correction), full pre-FSR (born level with kinematic acceptance correction), and non-diluted stage (parton level).

7.1 Distribution

Figures 7.1, 7.2, and 7.5 show the corrected P_{T}, invariant mass, $\cos\theta^*$, and rapidity distribution of dileptons. The central electrons are corrected for pile-up, energy scale, resolution and efficiency, and the pile-up and efficiency corrections are applied to the muons. In the case of forward electrons, the energy scale, resolution and efficiency correction are considered. As seen in Figures 7.1, 7.2, and 7.5, the tuned MC and the corrected data show excellent agreement. The slight difference at low P_{T} region is considered as a systematic error and discussed in Chapter 8.

7.2 Raw A_{FB}

7.2.1 Raw A_{FB} measured in Central Region

Figures 7.3 and 7.4 display the raw A_{FB} as a function of 12 mass bins in the electron and the muon channels. The bin edges are 40, 50, 60, 68, 75, 82, 88, 94, 100, 108, 140, 200,

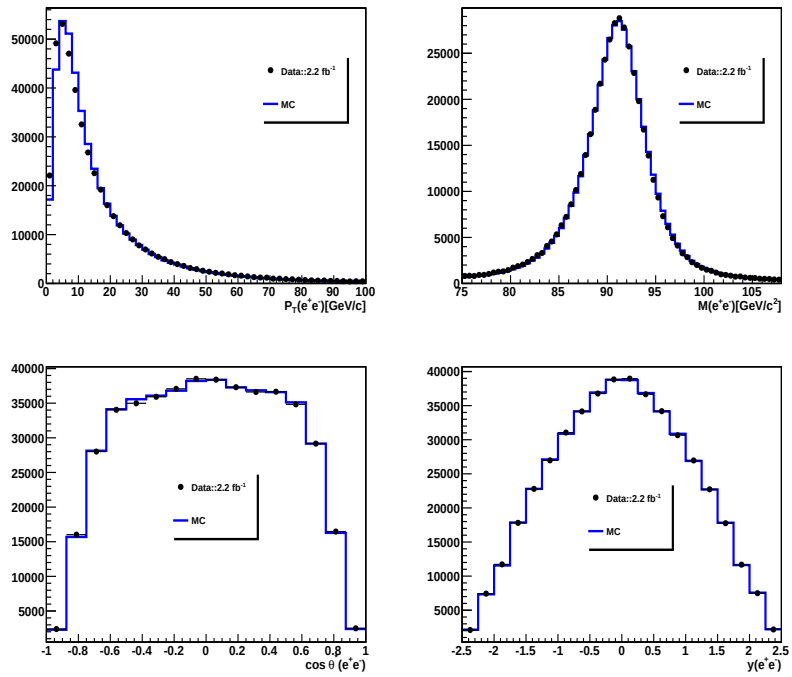

Figure 7.1: The corrected P_{T} (top left), $M_{e^+e^-}$ (top right), $\cos\theta^*$ (bottom left), and rapidity distribution (bottom right) of dielectron are shown.

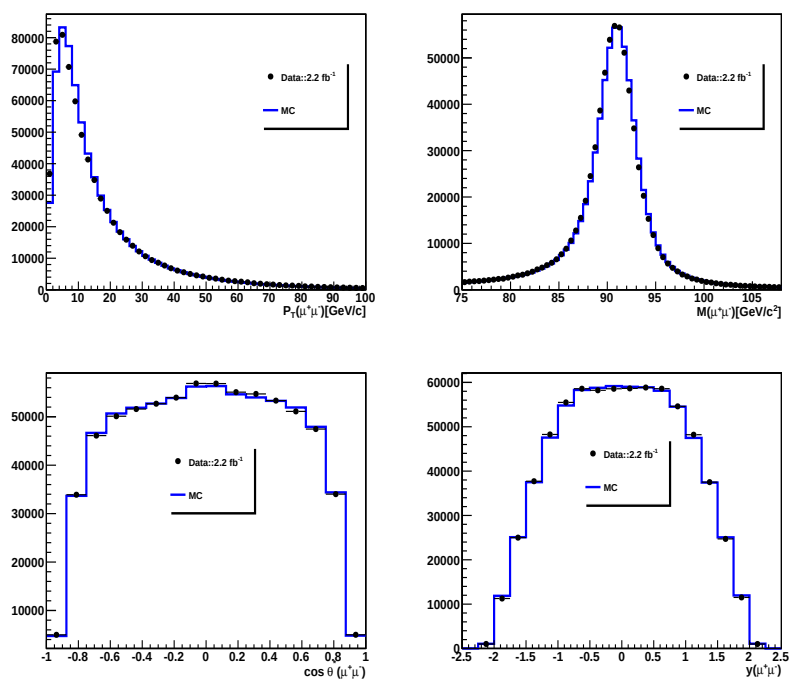

Figure 7.2: The corrected P_{T} (top left), $M_{\mu^+\mu^-}$ (top right), $\cos\theta^*$, (bottom left) and rapidity distribution (bottom right) of dimuon are shown.

1000 GeV/c^2. The expected A_{FB} is in solid blue line, and the measured A_{FB} is represented by black dots in these figures. The background is subtracted. As seen in Figures 7.3 and 7.4, the raw A_{FB} data and MC agreement is within statistical error. The statistical errors are given by

$$\Delta A_{\mathrm{FB}}(i) = \sqrt{\frac{1 - A_{\mathrm{FB}}^2}{N_i}} \tag{7.1}$$

where N_i is the total number of forward and backward events observed in each mass bin.

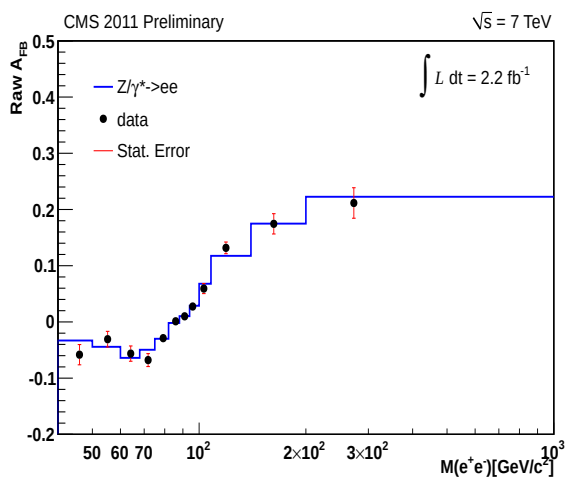

Figure 7.3: The raw A_{FB} is shown based on dielectrons in the central region. The blue solid line is the expected the A_{FB}, and the black circles are data with statistical errors.

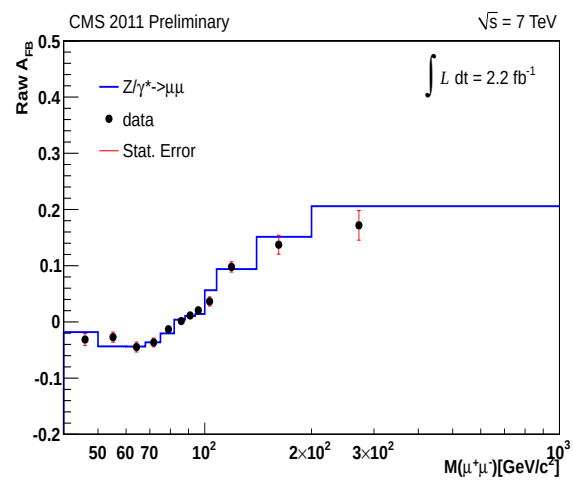

Figure 7.4: The raw A_{FB} is shown based on dimuons in the central region. The solid line in blue is the expected the A_{FB}, and the black circles are data with statistical errors.

7.2.2 Raw A_{FB} measured in the Forward Region

Figure 7.6 presents the raw A_{FB} with central and forward electron pairs with combined statistical and systematic uncertainties and shows a good agreement between the MC and data within uncertainties. We consider the background subtraction and the energy scale correction in this case. The most dominant background QCD is estimated with a limited MC sample size, and the energy scale correction ($\sim$ 22 %) is significant.

Figure 7.6 also shows the non-diluted A_{FB} (dash line). The raw A_{FB} values nearly reach the non-diluted values in high mass region because the dilutions are smaller when

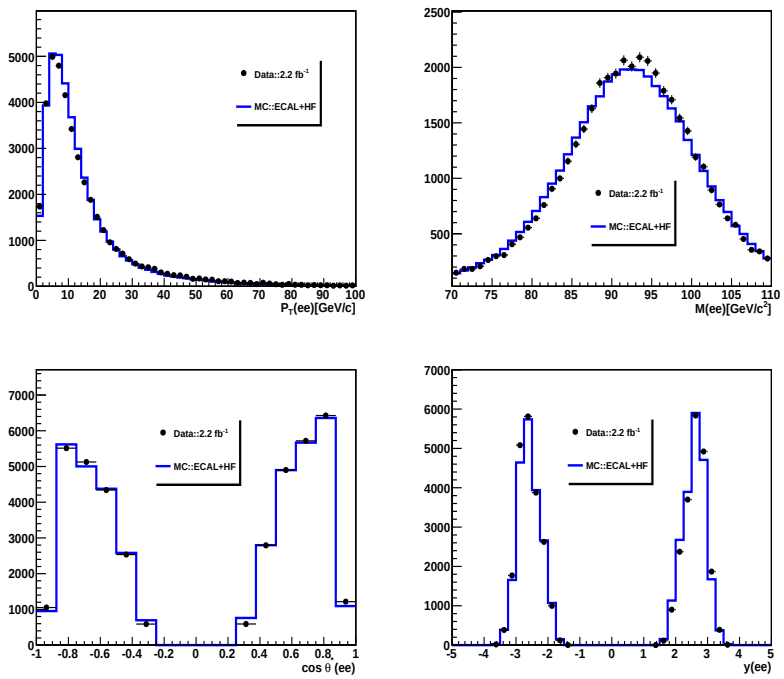

Figure 7.5: The corrected P_{T} (top left), M_{ee} (top right), $\cos\theta^*$ (bottom left), and rapidity distribution (bottom right) of central and forward electron are shown.

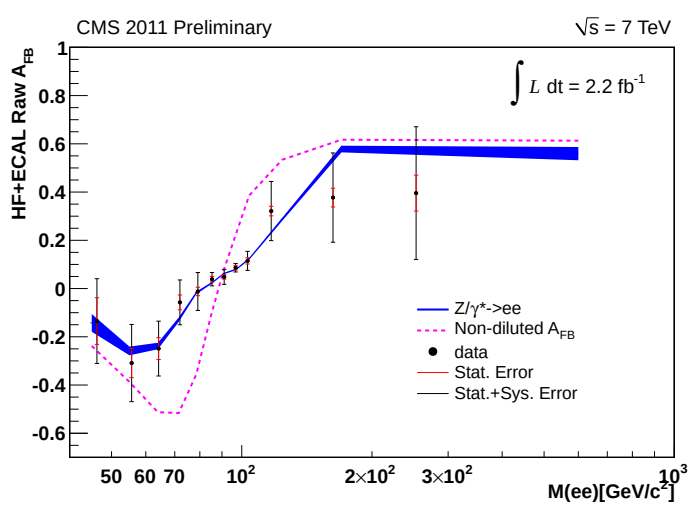

Figure 7.6: The raw A_{FB} with a central and forward electron pair. The statistical errors are in red and the combined statistical and systematic errors are in black. Background subtraction and the energy scale are considered to define systematic errors.

Table 7.1: The numerical values for the raw A_{FB} (central electron) are listed.

$M_{e^+e^-}$	$< M_{e^+e^-} >$	Expected A_{FB} (MC) $\pm$ Stat. Error	Raw A_{FB} (Data) $\pm$ Stat. Error
40-50	45.9	-0.033 ± 0.006	-0.058 ± 0.018
50-60	55.2	-0.044 ± 0.005	-0.030 ± 0.014
60-68	64.1	-0.063 ± 0.005	-0.056 ± 0.014
68-75	71.8	-0.049 ± 0.004	-0.067 ± 0.012
75-82	79.2	-0.030 ± 0.002	-0.028 ± 0.007
82-88	85.8	-0.001 ± 0.001	0.001 ± 0.003
88-94	91.0	0.010 ± 0.001	0.009 ± 0.001
94-100	95.9	0.028 ± 0.001	0.027 ± 0.003
100-108	103.1	0.067 ± 0.003	0.059 ± 0.009
108-140	119.0	0.118 ± 0.003	0.132 ± 0.010
140-200	162.4	0.175 ± 0.006	0.175 ± 0.018
200-1000	273.0	0.223 ± 0.010	0.212 ± 0.027

a forward electron is included in the measurement. CMS takes advantage of electrons in the forward calorimeter in order to measure model independent A_{FB} that is inherent in unfolding techniques.

7.3 Unfolding

7.3.1 Dilution Effects

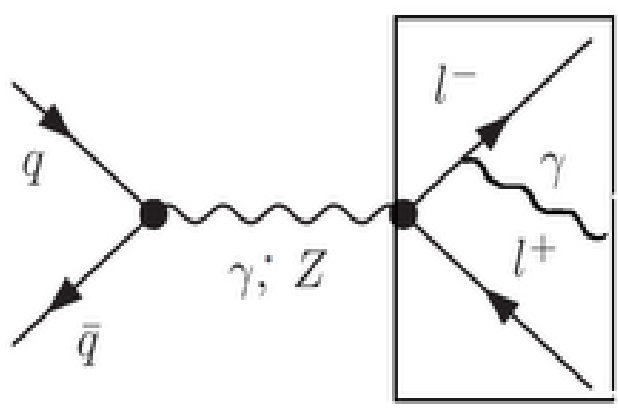

Figure 7.7: The born level of Drell-Yan process with FSR.

Table 7.2: The numerical values for the raw A_{FB} for dimuon are listed.

$M_{\mu^+\mu^-}$	$< M_{\mu^+\mu^-} >$	Expected A_{FB} (MC) $\pm$ Stat. Error	Raw A_{FB} (Data) $\pm$ Stat. Error
40-50	45.9	-0.018 ± 0.003	-0.031 ± 0.011
50-60	55.1	-0.043 ± 0.003	-0.027 ± 0.009
60-68	64.2	-0.043 ± 0.003	-0.044 ± 0.008
68-75	71.7	-0.036 ± 0.002	-0.036 ± 0.007
75-82	78.9	-0.020 ± 0.001	-0.013 ± 0.005
82-88	85.8	0.004 ± 0.001	0.001 ± 0.003
88-94	90.9	0.010 ± 0.001	0.011 ± 0.001
94-100	95.8	0.014 ± 0.001	0.020 ± 0.003
100-108	103.2	0.056 ± 0.002	0.036 ± 0.008
108-140	118.9	0.094 ± 0.003	0.097 ± 0.009
140-200	161.6	0.151 ± 0.005	0.137 ± 0.017
200-1000	272.0	0.206 ± 0.009	0.172 ± 0.026

The main dilution factors in A_{FB} measurement are the following:

1. detector mass resolution,
2. kinematic and geometric acceptance,
3. quantum electrodynamics Final State Radiation (FSR), and
4. the unknown quark direction.

Due to FSR, invariably energy is lost in reconstructing the invariant masses, especially apparent at the Z pole, and it induces bin-to-bin mass migration, and therefore dilution in asymmetry.

To correct this diluted A_{FB}, MC samples are used for building a correlation between the reconstructed and generated before the FSR process (pre-FSR). First, we unfold the A_{FB} to the pre-FSR stage. This is followed by an additional correction based on quark direction using MC.

7.3.2 Unfolding Procedure

The simple matrix inversion method is a part of unfolding procedure in this analysis. The first step is to build the response matrices which contain the correlation between the de-

tected dilepton and the generated dilepton mass with respect to forward/backward events. R_{FF} stands for forward event in both generated and reconstructed level, and R_{BF} is for backward event in generation and forward event in reconstructed level. The same rule is applied to R_{FB} and R_{BB}. Each response matrix is filled with generated pre-FSR dilepton mass in x-axis and reconstructed mass in y-axis based on simulated MC. We build 4 two dimensional response matrices. The pre-FSR leptons are collected to forward and backward events into obtain an expected A_{FB} value, and the response matrices are normalized as shown:

$$R_{ij}^{\mathrm{FF}} = \frac{N_j^{\mathrm{F}}(\mathrm{Reco})}{N_i^{\mathrm{F}}(\mathrm{Gen})},\ R_{ij}^{\mathrm{FB}} = \frac{N_j^{\mathrm{B}}(\mathrm{Reco})}{N_i^{\mathrm{F}}(\mathrm{Gen})} \tag{7.2}$$

$$R_{ij}^{\mathrm{BF}} = \frac{N_j^{\mathrm{F}}(\mathrm{Reco})}{N_i^{\mathrm{B}}(\mathrm{Gen})},\ R_{ij}^{\mathrm{BB}} = \frac{N_j^{\mathrm{B}}(\mathrm{Reco})}{N_i^{\mathrm{B}}(\mathrm{Gen})}. \tag{7.3}$$

where $N_j^{\mathrm{F}}(\mathrm{Reco})$ ($N_j^{\mathrm{B}}(\mathrm{Reco})$) is the number of forward (backward) events reconstructed in the j-th of $M_{l^+l^-}$, and $N_i^{\mathrm{F}}(\mathrm{Gen})$ ($N_i^{\mathrm{B}}(\mathrm{Gen})$) is the number of forward (backward) events generated in the j-th of $M_{l^+l^-}$. i and j represent mass bins.

We evaluate the response matrix in two stages: limited pre-FSR stage that we use only reconstructed dileptons with kinematic selection and their generated dileptons, and full pre-FSR stage that all generated events are used for kinematic acceptance correction. Then we invert the normalized response matrices and apply them to reconstructed leptons.

7.3.3 Limited Pre-FSR A_{FB} Stage

To minimize model dependence, only reconstructed dileptons and their generated dileptons are included in response matrices. The four response matrices are shown in Figures 7.8 and 7.9. Even though R_{FB} and R_{BF} are maps of reconstructed to generated event, only R_{FF} and R_{BB} are used in unfolding to pre-FSR A_{FB} since R_{FF} and R_{BB} are dominant compared to R_{FB} and R_{BF} (R_{FB} and R_{BF} are about 4%).

To see this effect and to check the unfolding inversion process, a closure test is per-

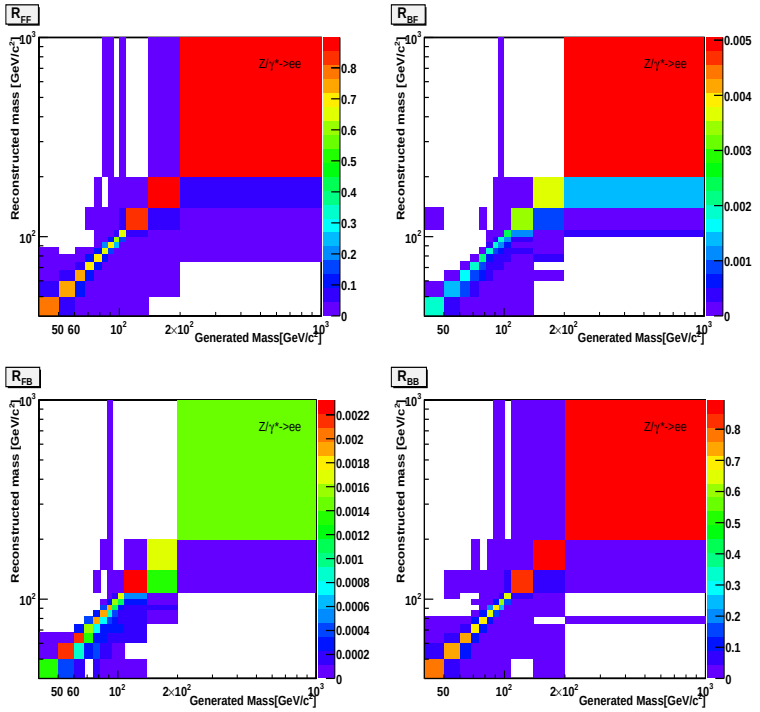

Figure 7.8: Response matrices in the electron channel.

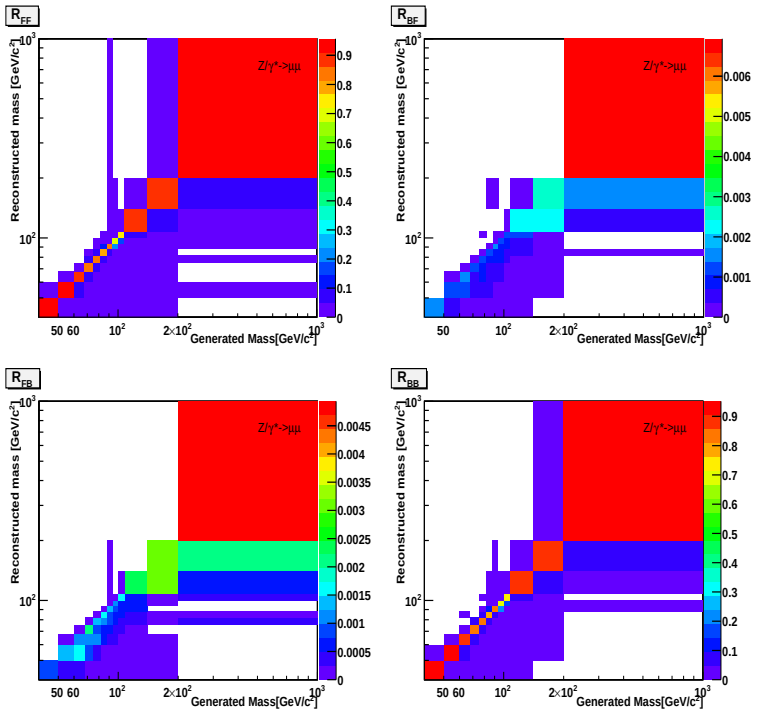

Figure 7.9: Response matrices in the muon channel.

formed with the simulated data. In Figure 7.10, the solid line is the *true* value based on the exact unfolding process, and the dots are the result of unfolding with only R_{FF} and R_{BB}. As seen in Figure 7.10, a simple inversion with R_{FF} and R_{BB} can achieve the desired result without including significant error in A_{FB}. The unfolded results are shown in Figures 7.11 (dielectrons) and 7.12 (dimuons).

In this analysis, the statistical errors are evaluated by 1000 pseudo-experiment toys. First, 1000 toys are randomly selected in MC in order to have the same number of events as data. Then, we fill A_{FB} into 12 histograms which are indicated with respect to 12 mass regions. Finally, the RMS in each plot is referred as statistical error. Figure 7.13 shows 12 plots as a function of A_{FB}, and each plots represents 12 mass bin. Table 7.5 shows statistical errors comparison between the pseudo-experiments and calculated by Equation 7.1.

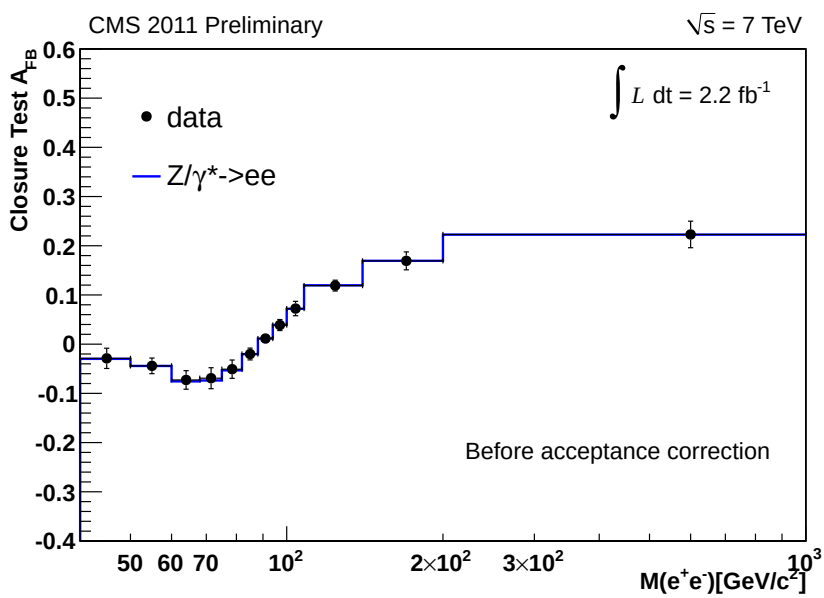

Figure 7.10: Closure test in the electron channel.

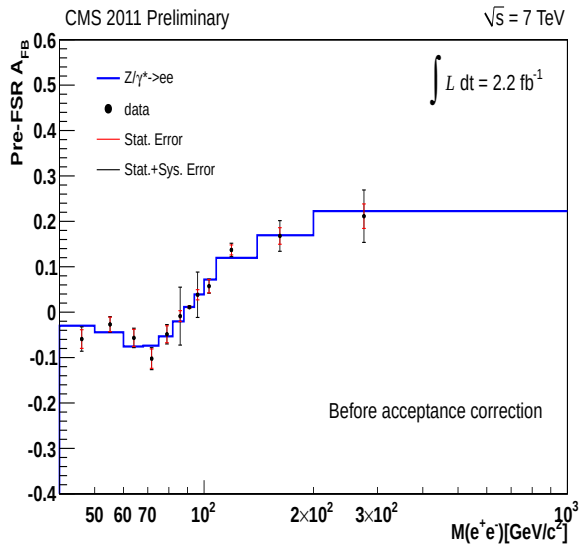

Figure 7.11: Unfolded A_{FB} to the limited pre-FSR electron stage.

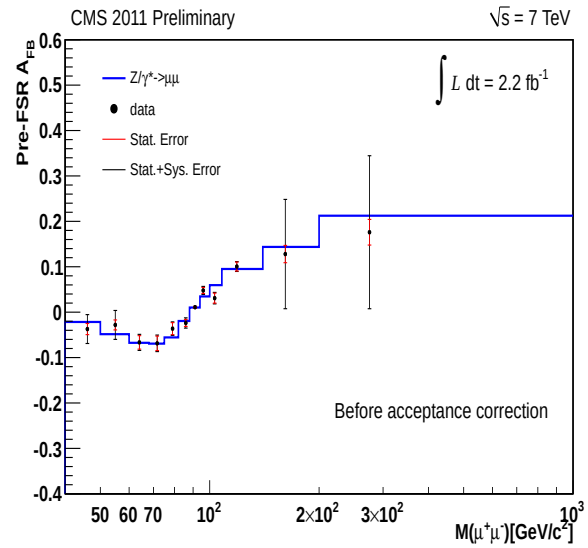

Figure 7.12: Unfolded A_{FB} to limited pre-FSR muon stage.

7.3.4 Full Pre-FSR A_{FB} Stage

To unfold to full pre-FSR stage A_{FB}, information of all generated pre-FSR lepton is used for the normalizing matrices. The normalized response matrices for full pre-FSR stage are shown in Figures 7.14 and 7.15. R_{FF} and R_{BB} are used for unfolding to pre-FSR A_{FB}, and closure tests are performed (see Figure 7.16). Final unfolding A_{FB} result to full pre-FSR lepton stage is in Figures 7.17 and 7.18.

7.3.5 A_{FB}, $|y| > 1$

The usage of high rapidity regions can effectively suppress dilution effect. Since more dilution is expected near zero rapidity of dilepton, event selection of $|y| > 1$ can achieve less-diluted A_{FB}. The unfolding procedures in the limited and full pre-FSR stages with a selection of $|y| > 1$. Figures 7.19 and 7.20 show limited pre-FSR A_{FB} with selection of $|y| > 1$ is repeated to minimize dilution, and Figures 7.21 and 7.22 present a full pre-FSR A_{FB} with high rapidity dilepton. They are clearly less-diluted as compared to the previous results. Figures are with statistical errors only, A_{FB} estimated by pseudo-experiments.

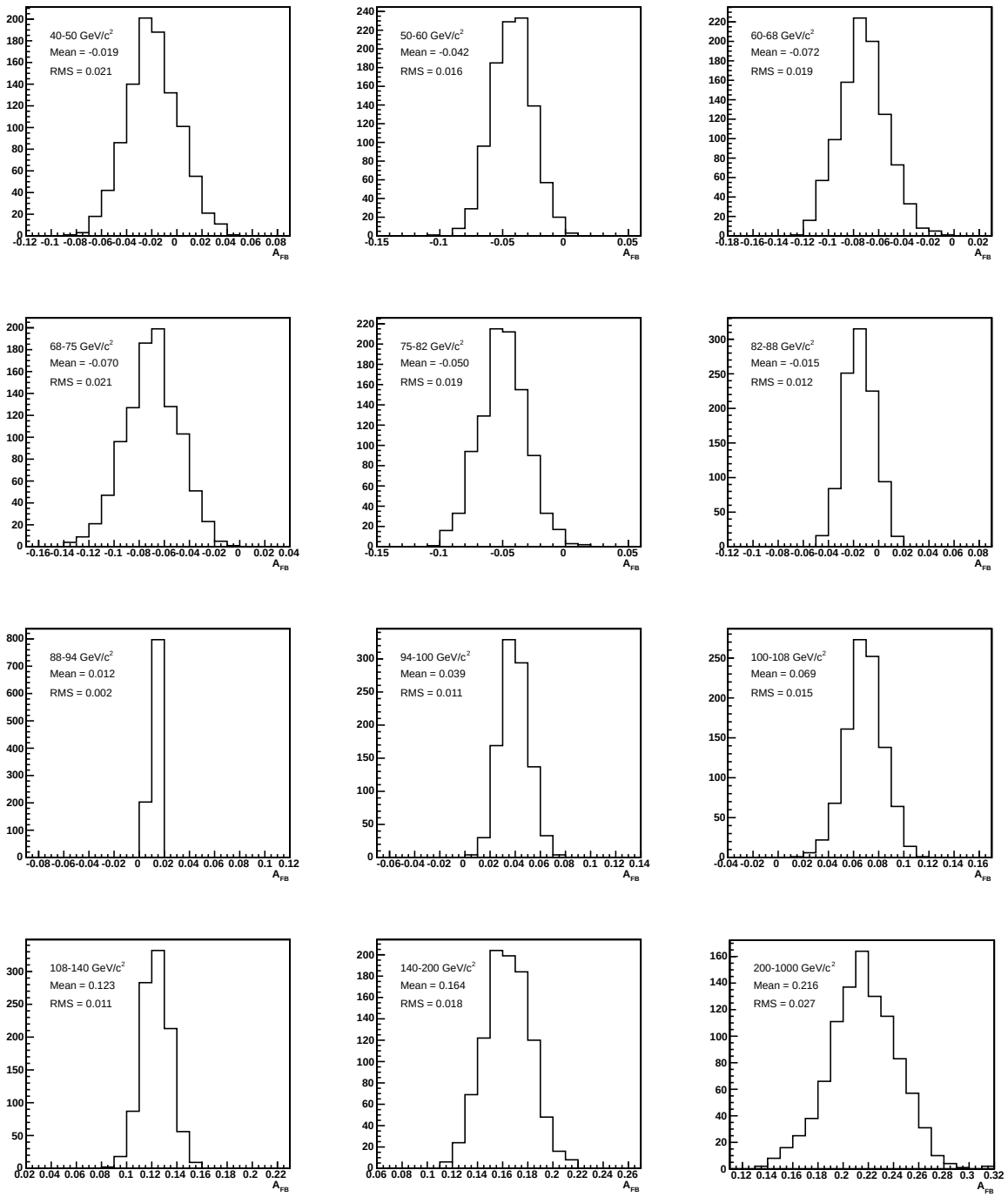

Figure 7.13: A_{FB} is tested in 12 mass regions with 1000 pseudo-experimental toys to evaluated the statistical errors.

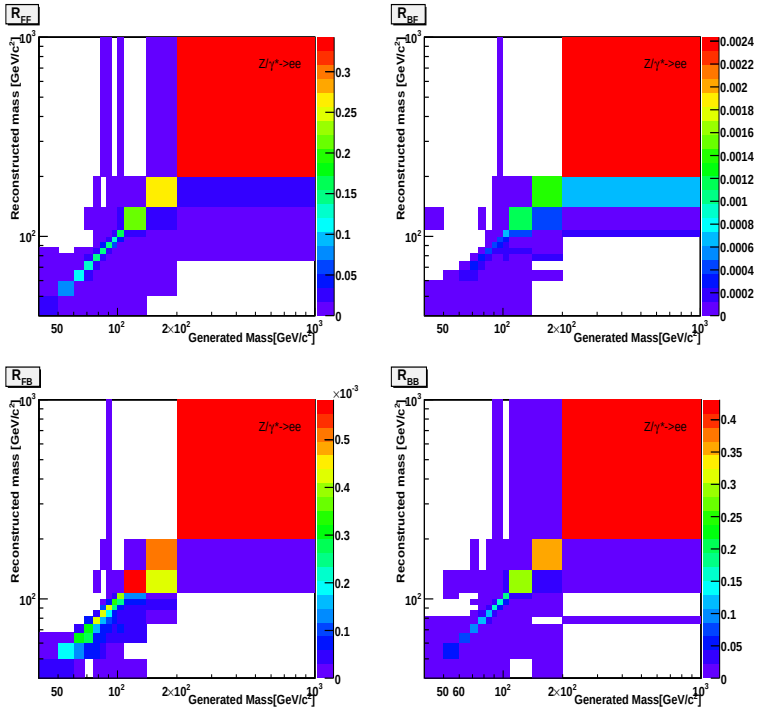

Figure 7.14: The response matrices are normalized by all generated events in order to unfold to full pre-FSR stage in the electron channel.

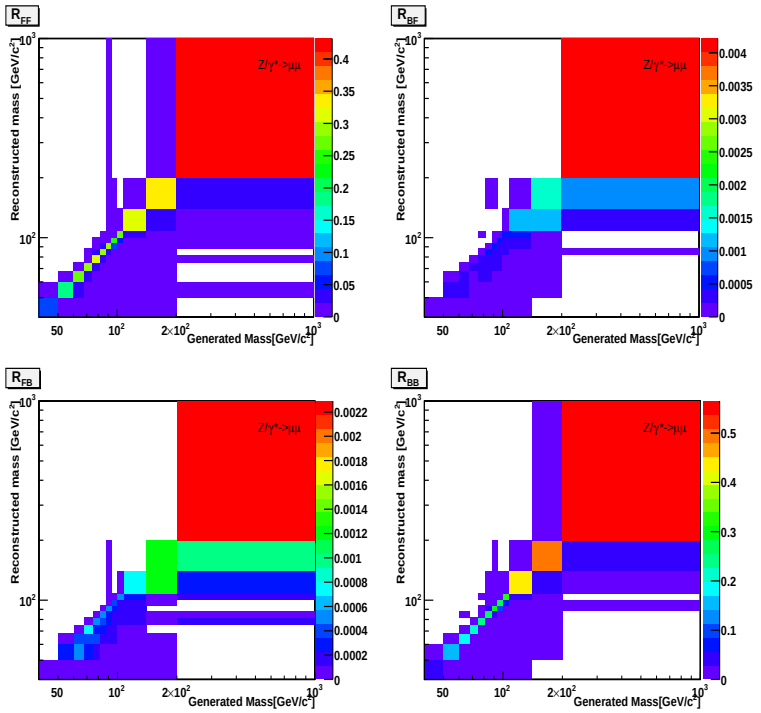

Figure 7.15: Response matrices are normalized by all generated events in order to unfold to full pre-FSR stage in the muon channel.

Table 7.3: Unfolded A_{FB} to limited pre-FSR electron stage in electron.

$M_{e^+e^-}$	$< M_{e^+e^-} >$	Expected A_{FB}	pre-FSR $A_{\mathrm{FB}} \pm$ Error	Stat. Error / Syst. Error
40-50	46.0	-0.029	-0.059 ± 0.027	± 0.021 ± 0.017
50-60	55.1	-0.044	-0.027 ± 0.017	± 0.016 ± 0.006
60-68	64.1	-0.075	-0.056 ± 0.021	± 0.019 ± 0.010
68-75	71.7	-0.073	-0.102 ± 0.024	± 0.021 ± 0.011
75-82	79.0	-0.053	-0.048 ± 0.021	± 0.019 ± 0.010
82-88	85.9	-0.020	-0.008 ± 0.063	± 0.012 ± 0.062
88-94	91.1	0.011	0.011 ± 0.002	± 0.002 ± 0.001
94-100	95.9	0.039	0.038 ± 0.050	± 0.011 ± 0.049
100-108	103.2	0.071	0.057 ± 0.016	± 0.015 ± 0.005
108-140	118.9	0.120	0.137 ± 0.015	± 0.011 ± 0.009
140-200	161.7	0.169	0.168 ± 0.034	± 0.018 ± 0.028
200-1000	275.5	0.223	0.211 ± 0.058	± 0.027 ± 0.051

7.3.6 Non-diluted A_{FB}

To obtain non-diluted A_{FB}, we rely on NLO MC in order to define *true* quark direction. The *true* quark direction is defined by generated particle information in POWHEG. In POWHEG stored mothers of Z are a pair of quark and anti-quark, quark and gluon, and gluon and anti-quark. We take account of all pairs of quark and anti-quark, quark and gluon, and gluon and anti-quark to define dilution. Therefore, the direction of quark or gluon (another pair of anti-quark) is referred to the quark direction.

The unfolding A_{FB} to pre-FSR stage is performed under the assumption that the direction of dilepton matches the quark direction, because the quark direction is unknown at the LHC. This correction is required to get to the *true* A_{FB}. First we investigate how frequently the pre-FSR dilepton direction does not match to quark direction. Define D_{BF} as *true* forward events determined as backward events normalized by total number of events and D_{FB} as *true* backward events determined as forward events normalized by total number of events. Then, the non-diluted forward/backward events are corrected by the following equations:

Table 7.4: Unfolded A_{FB} to limited pre-FSR electron stage in muon.

$M_{\mu^+\mu^-}$	$< M_{\mu^+\mu^-} >$	Expected A_{FB}	pre-FSR $A_{\mathrm{FB}} \pm$ Error	Stat. Error / Syst. Error
40-50	46.0	-0.021	-0.037 ± 0.032	± 0.012 ± 0.029
50-60	54.9	-0.048	-0.028 ± 0.032	± 0.011 ± 0.030
60-68	64.0	-0.067	-0.066 ± 0.018	± 0.015 ± 0.009
68-75	71.7	-0.069	-0.068 ± 0.018	± 0.016 ± 0.008
75-82	79.0	-0.055	-0.036 ± 0.015	± 0.013 ± 0.006
82-88	85.9	-0.019	-0.023 ± 0.012	± 0.007 ± 0.009
88-94	91.1	0.010	0.011 ± 0.001	± 0.001 ± 0.001
94-100	95.9	0.034	0.047 ± 0.009	± 0.006 ± 0.006
100-108	103.2	0.059	0.030 ± 0.013	± 0.011 ± 0.006
108-140	118.7	0.095	0.100 ± 0.011	± 0.009 ± 0.004
140-200	161.5	0.144	0.128 ± 0.120	± 0.019 ± 0.120
200-1000	275.3	0.212	0.176 ± 0.170	± 0.028 ± 0.170

$$F_i^{\mathrm{T}} = F_i^{\mathrm{pre-FSR}} - D_{\mathrm{BF}} \times (F_i^{\mathrm{T}} + B_i^{\mathrm{T}}) + D_{\mathrm{FB}} \times (F_i^{\mathrm{T}} + B_i^{\mathrm{T}}) \tag{7.4}$$

$$B_i^{\mathrm{T}} = B_i^{\mathrm{pre-FSR}} - D_{\mathrm{FB}} \times (F_i^{\mathrm{T}} + B_i^{\mathrm{T}}) + D_{\mathrm{BF}} \times (F_i^{\mathrm{T}} + B_i^{\mathrm{T}}) \tag{7.5}$$

where F_i^{T} and B_i^{T} are the non-diluted forward and backward events in mass bin i, and $F_i^{\mathrm{pre-FSR}}$ and $B_i^{\mathrm{pre-FSR}}$ are pre-FSR forward and backward events in mass bin i. The dilution rates D_{BF} and D_{FB} are listed in Table 7.8, and its closure test is shown in Figure 7.23. Non-diluted A_{FB} with corrected forward and backward is shown in Figures 7.24 and 7.25, and they are consistent with the SM prediction within uncertainties.

We obtain non-diluted A_{FB}, the same as *true*, in dielectron and dimuon channels. Therefore, Figures 7.24 and 7.25 can be combined. In Figure 7.26, the *true* A_{FB} predicted by the SM is in solid line, and the non-diluted A_{FB} results are combined and shown in data points with uncertainties. The combined non-diluted A_{FB} also shows good agreement with the SM prediction within uncertainties.

Table 7.5: The statistical error comparison is shown in the electron and muon channels. N_i is observed events here.

$M_{l^+l^-}$	Electron (Toy)	Electron ($\sqrt{\frac{1-A_{FB}^2}{N_i^*}}$)	Muon (Toy)	Muon ($\sqrt{\frac{1-A_{FB}^2}{N_i^*}}$)
40-50	0.021	0.018	0.012	0.011
50-60	0.016	0.014	0.011	0.009
60-68	0.019	0.014	0.015	0.008
68-75	0.021	0.011	0.016	0.007
75-82	0.019	0.007	0.013	0.005
82-88	0.012	0.003	0.007	0.003
88-94	0.002	0.001	0.001	0.001
94-100	0.011	0.003	0.006	0.003
100-108	0.015	0.009	0.011	0.008
108-140	0.011	0.010	0.009	0.009
140-200	0.018	0.018	0.019	0.017
200-1000	0.027	0.027	0.028	0.026

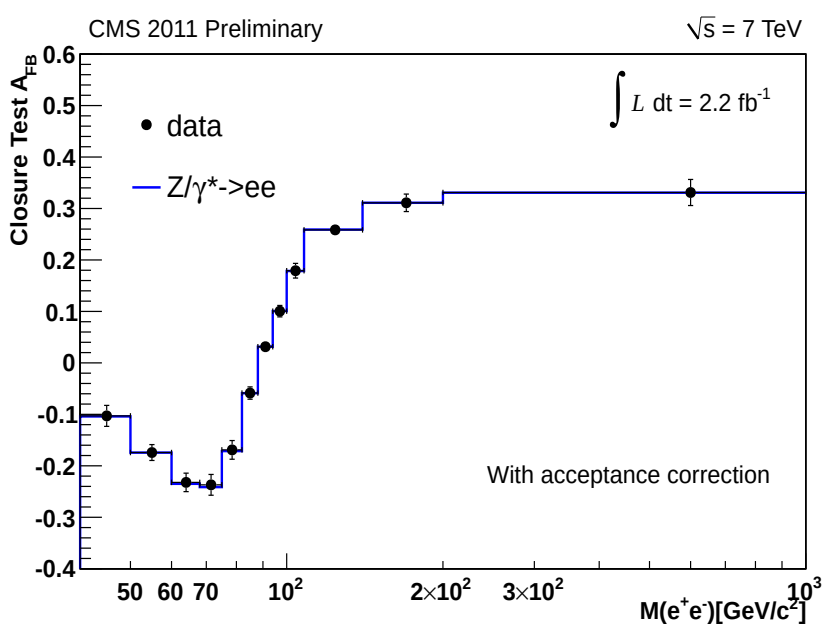

Figure 7.16: The inversion process for unfolding to all pre-FSR stage is checked by a closure test with reconstructed electron in MC.

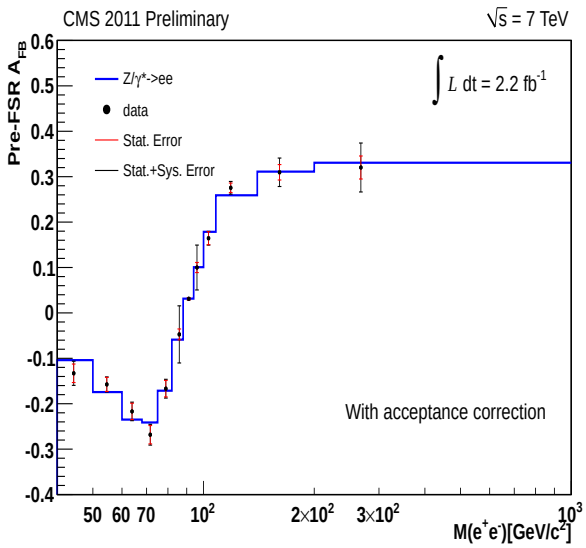

Figure 7.17: Unfolded A_{FB} to all pre-FSR electron stage.

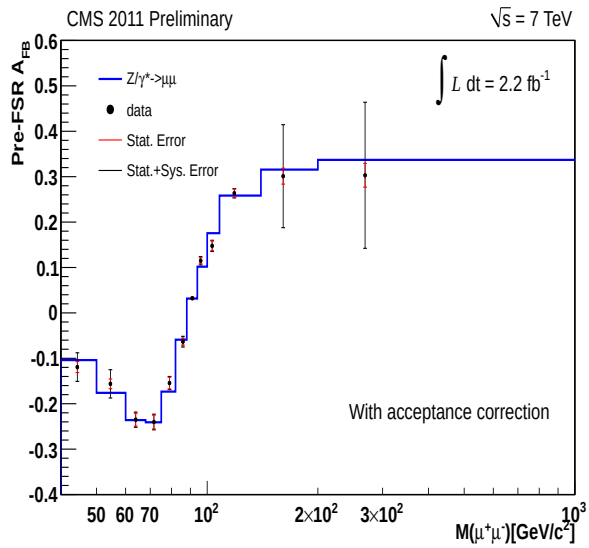

Figure 7.18: Unfolded A_{FB} to all pre-FSR muon stage.

Table 7.6: Unfolded A_{FB} to pre-FSR stage with acceptance correction for electron.

$M_{e^+e^-}$	$< M_{e^+e^-} >$	Expected A_{FB}	pre-FSR $A_{\mathrm{FB}} \pm$ Error	Stat. Error / Syst. Error
40-50	44.3	-0.104	-0.133 ± 0.027	± 0.020 ± 0.017
50-60	54.5	-0.174	-0.157 ± 0.017	± 0.015 ± 0.006
60-68	63.9	-0.235	-0.217 ± 0.020	± 0.018 ± 0.009
68-75	71.6	-0.241	-0.268 ± 0.023	± 0.020 ± 0.011
75-82	78.9	-0.171	-0.167 ± 0.021	± 0.018 ± 0.009
82-88	85.9	-0.058	-0.047 ± 0.063	± 0.012 ± 0.062
88-94	91.1	0.031	0.031 ± 0.002	± 0.002 ± 0.001
94-100	95.9	0.101	0.099 ± 0.049	± 0.011 ± 0.048
100-108	103.2	0.179	0.164 ± 0.015	± 0.014 ± 0.005
108-140	118.5	0.259	0.275 ± 0.014	± 0.010 ± 0.009
140-200	160.9	0.311	0.310 ± 0.031	± 0.017 ± 0.026
200-1000	267.8	0.331	0.320 ± 0.054	± 0.025 ± 0.048

Table 7.7: Unfolded A_{FB} to pre-FSR stage with acceptance correction for muon.

$M_{\mu^+\mu^-}$	$< M_{\mu^+\mu^-} >$	Expected A_{FB}	pre-FSR $A_{\mathrm{FB}} \pm$ Error	Stat. Error / Syst. Error
40-50	44.3	-0.104	-0.119 ± 0.031	± 0.012 ± 0.029
50-60	54.5	-0.176	-0.156 ± 0.031	± 0.011 ± 0.029
60-68	63.9	-0.236	-0.235 ± 0.017	± 0.014 ± 0.009
68-75	71.6	-0.241	-0.240 ± 0.017	± 0.015 ± 0.008
75-82	78.9	-0.173	-0.154 ± 0.014	± 0.013 ± 0.006
82-88	85.9	-0.059	-0.063 ± 0.012	± 0.007 ± 0.008
88-94	91.1	0.031	0.032 ± 0.001	± 0.001 ± 0.001
94-100	95.9	0.102	0.115 ± 0.009	± 0.006 ± 0.006
100-108	103.2	0.176	0.148 ± 0.012	± 0.011 ± 0.006
108-140	118.5	0.258	0.263 ± 0.010	± 0.009 ± 0.004
140-200	160.9	0.316	0.301 ± 0.110	± 0.018 ± 0.110
200-1000	268.8	0.337	0.303 ± 0.160	± 0.026 ± 0.160

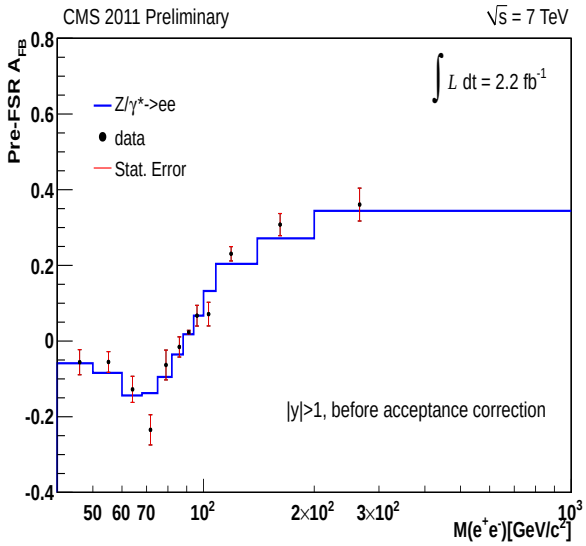

Figure 7.19: Unfolding A_{FB} to limited pre-FSR stage in the electron channel with $|y| > 1$ cut.

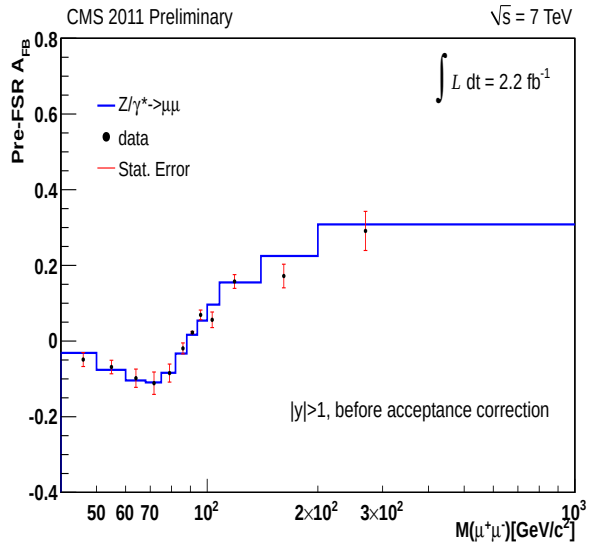

Figure 7.20: Unfolding A_{FB} to limited pre-FSR stage in the muon channel with $|y| > 1$ cut.

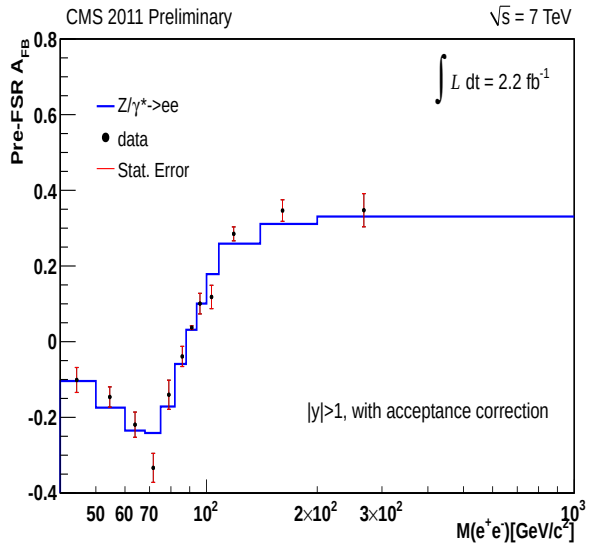

Figure 7.21: Unfolding A_{FB} to all pre-FSR stage in the electron channel with $|y| > 1$ cut.

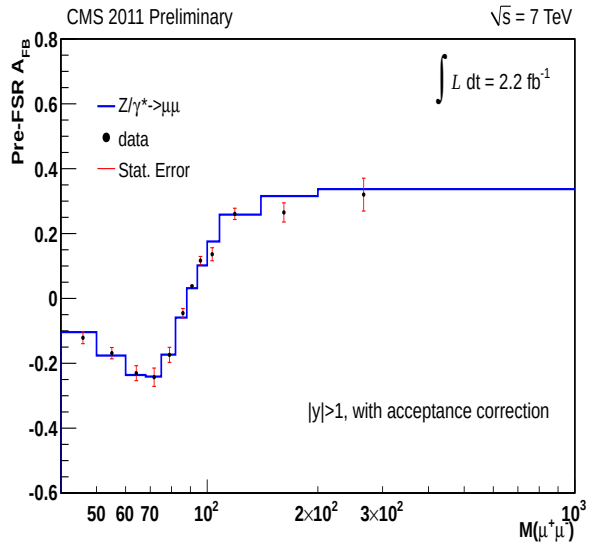

Figure 7.22: Unfolding A_{FB} to all pre-FSR stage in the muon channel with $|y| > 1$ cut.

Table 7.8: Dilution rates of D_{BF} and D_{FB} in the electron and muon channels.

$M_{l^+l^-}$	Dielectron D_{BF}	Dielectron D_{FB}	Dimuon D_{BF}	Dimuon D_{FB}
40-50	0.094	0.162	0.094	0.161
50-60	0.077	0.184	0.077	0.183
60-68	0.065	0.204	0.064	0.205
68-75	0.070	0.208	0.070	0.207
75-82	0.097	0.190	0.097	0.189
82-88	0.134	0.159	0.134	0.159
88-94	0.159	0.134	0.159	0.134
94-100	0.176	0.113	0.176	0.113
100-108	0.195	0.091	0.195	0.091
108-140	0.205	0.068	0.206	0.066
140-200	0.204	0.050	0.202	0.049
200-1000	0.187	0.045	0.187	0.044

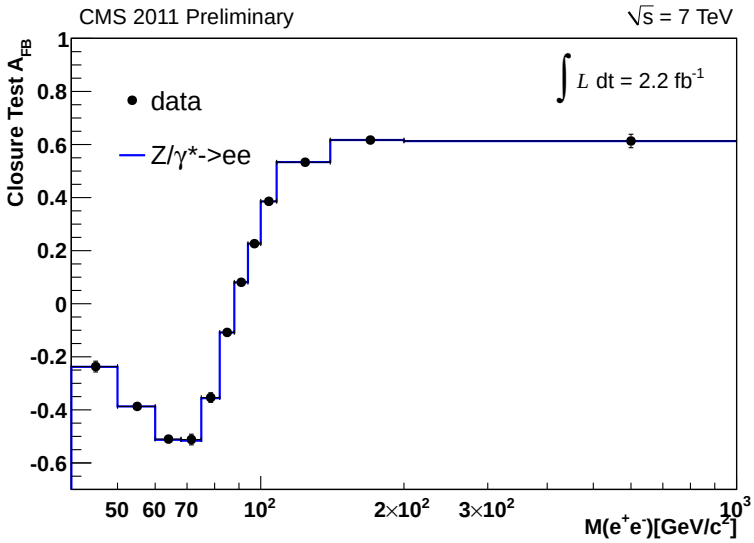

Figure 7.23: Closure test in the electron channel for unfolding to non-diluted stage.

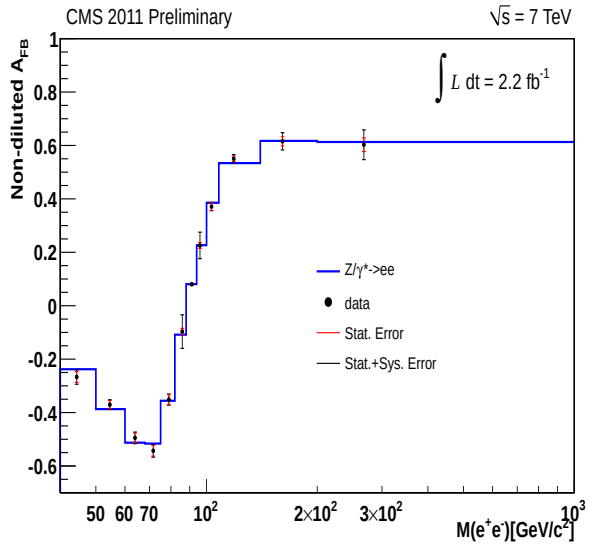

Figure 7.24: Unfolded A_{FB} to non-diluted stage in the electron channel.

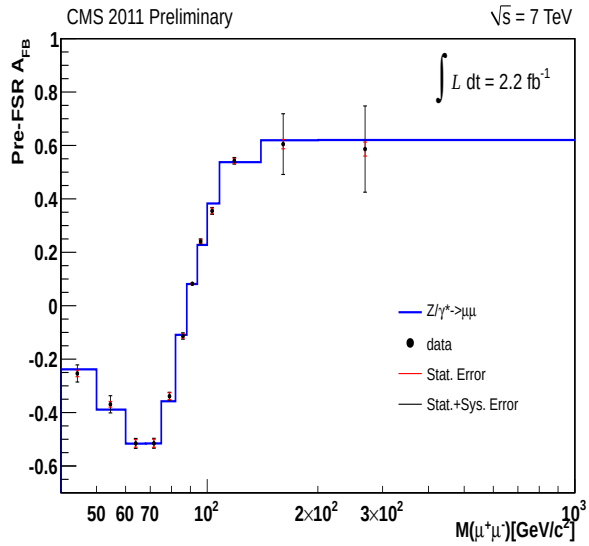

Figure 7.25: Unfolded A_{FB} to non-diluted stage in the muon channel.

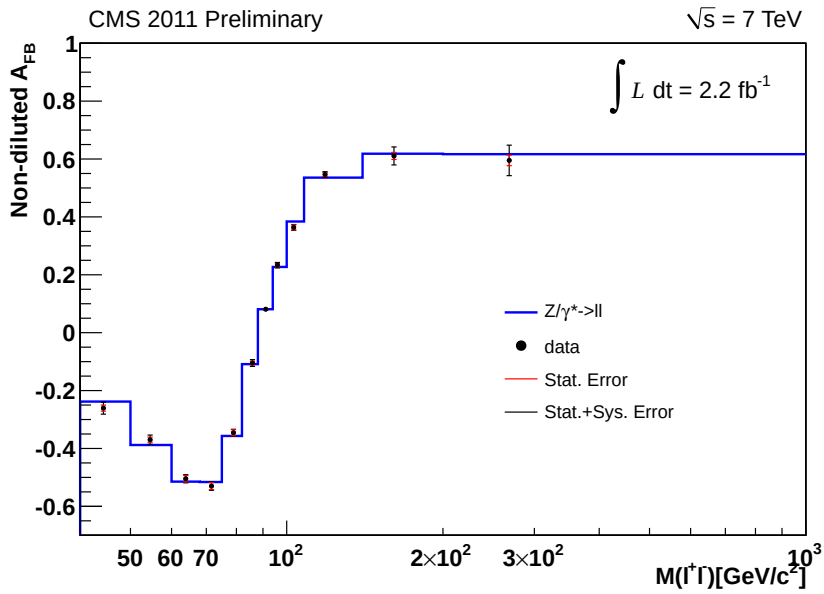

Figure 7.26: Unfolded A_{FB} to non-diluted stage in the lepton channel.

Chapter 8

Systematics

Systematic uncertainties (ΔA_{FB}) are evaluated using MC samples. ΔA_{FB} is defined as

$$\Delta A_{\mathrm{FB}} = A^{c}_{\mathrm{FB}} - A^{t}_{\mathrm{FB}} \tag{8.1}$$

where A^{c}_{FB} is the corrected whereas A^{t}_{FB} represents the value of A_{FB} under test.

8.1 Pile-up

Table 5.4 shows the re-weighting factors to tune MC in the electron and muon channels. To define pile-up systematic error, A^{c}_{FB} is found with pile-up tuned MC, and A^{t}_{FB} is without the re-weighting factors on the number of vertices. Figure 8.1 summarizes the pile-up systematic error.

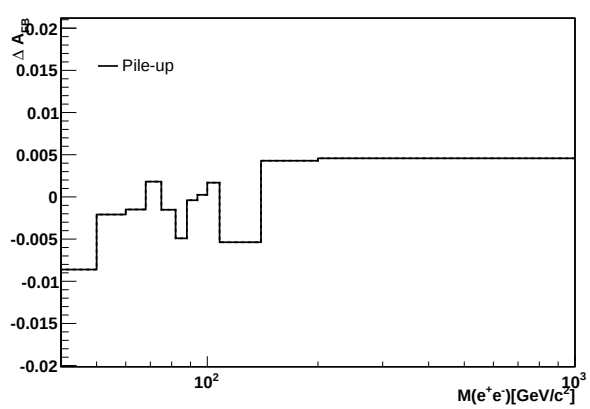

Figure 8.1: Systematic uncertainty of pile-up in the electron channel.

8.2 Efficiency

In this analysis, double triggered lepton data sets are used. Since it is hard to get non-biased HLT trigger efficiency from the double triggered data sets, only the identification efficiency is used. Therefore, the efficiency uncertainty in Figure 8.2 is calculated by efficiency-corrected A^c_{FB} and tested A^t_{FB}.

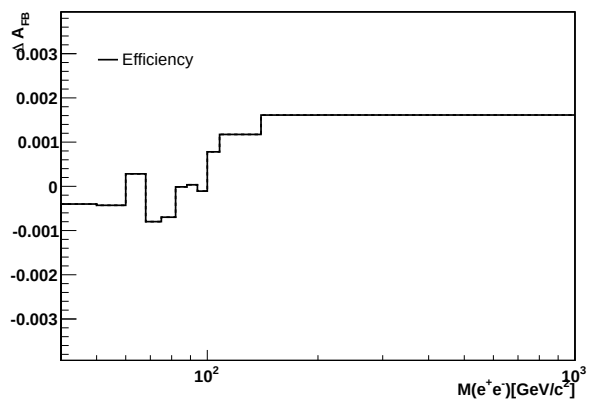

Figure 8.2: Systematic uncertainty of efficiency in the electron channel.

8.3 Energy Scale and Resolution

8.3.1 Electron

We apply energy scale and resolution correction to ensure data/MC agreement. The correction factors are found by a χ^2 test. The correction errors are assigned by allowing the χ^2 to increase by 1. In order to define systematic uncertainty in energy scale and resolution in the electron channel, we take into account maximum correction errors.

For the central electrons, the maximum correction error is about 0.2% for the energy scale and is about 0.5% for the energy smearing. We examine A_{FB} with 0.2% energy scale up (referring to A^t_{FB}) and calculated ΔA_{FB}. In Figure 8.3, the solid line is ΔA_{FB} with energy scale up and the dashed line is for energy scale down. The larger differences in each mass bin are chosen for systematic uncertainty. The systematic uncertainty of energy smearing

also found the same procedure with maximum error 0.5%. (see Figure 8.5)

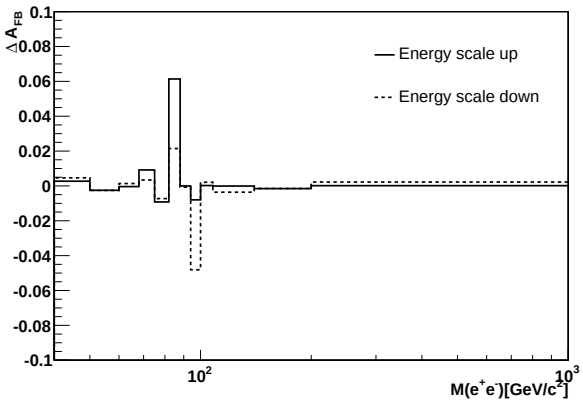

Figure 8.3: Systematic uncertainty of energy scale in the electron channel.

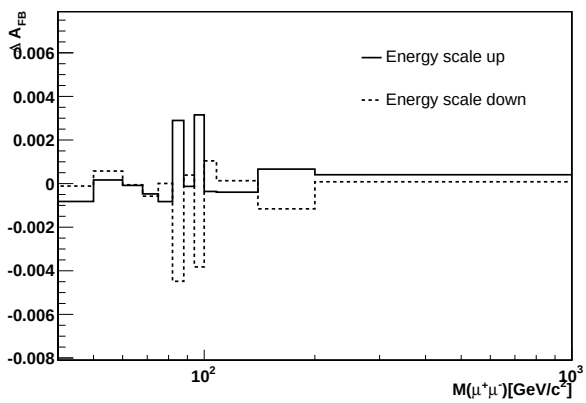

Figure 8.4: Systematic uncertainty of energy scale in the muon channel.

Energy smearing factor is applied to tune MC. Smearing factors are found using χ^2 test, and their errors are less than 0.5%. Systematic uncertainty of energy resolution in the electron channel takes account of 0.5% up and down effect on A_{FB} using simulated MC.

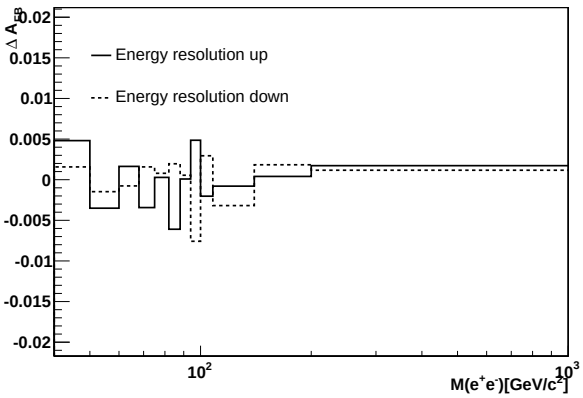

Figure 8.5: Systematic uncertainty of energy resolution in the electron channel.

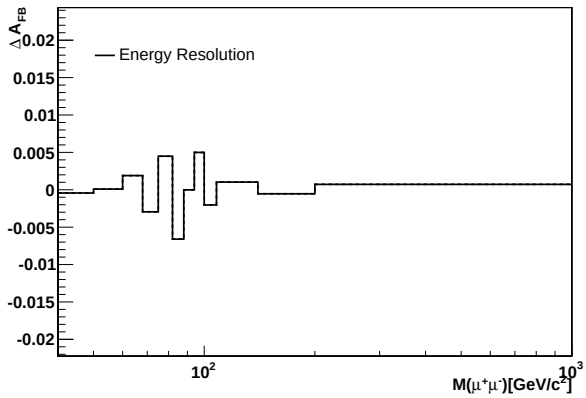

Figure 8.6: Systematic uncertainty of energy resolution in the muon channel.

8.3.2 Muon

As seen in Figure 5.4 the shape of invariant mass distributions for dimuons is slightly off compared to the MC. However, the energy scale and resolution correction are not applied

because their effects on A_{FB} are not significant. The energy scale and resolution correction factors are found using the same method as electron. Then, the larger difference of A_{FB} with correction scale up and down is taken for systematic uncertainty of energy scale, and the simple deviation of A_{FB} with/without resolution correction is defined as systematic uncertainty of resolution (see Figure 8.4 and 8.6). Table 8.1 is shown the energy scale and resolution correction with respect to η bins.

Table 8.1: The energy scale and resolution correction with respect to η bins.

	$-2.1< \eta < -2.0$	$-2.0< \eta < -1.5$	$-1.5< \eta < -1.0$	$-1.0< \eta < -0.5$	$-0.5< \eta <0.0$
Scale	1.00539	1.00009	1.00056	1.00188	1.00094
Res	0.0400	0.0160	0.0035	0.0000	0.0025
	$0.0< \eta <0.5$	$0.5< \eta <1.0$	$1.0< \eta <1.5$	$1.5< \eta <2.0$	$2.0< \eta <2.1$
Scale	1.00139	1.00126	1.00140	1.00127	0.99544
Res	0.0015	0.0070	0.0085	0.0040	0.0045

8.4 Background

Background events are counted in 12 mass bins. Systematic uncertainty of background subtraction is defined as the larger difference between $+$ 100% and $-$ 100 % from signal MC A_{FB}. Systematic uncertainty of background subtraction is in Figure 8.7.

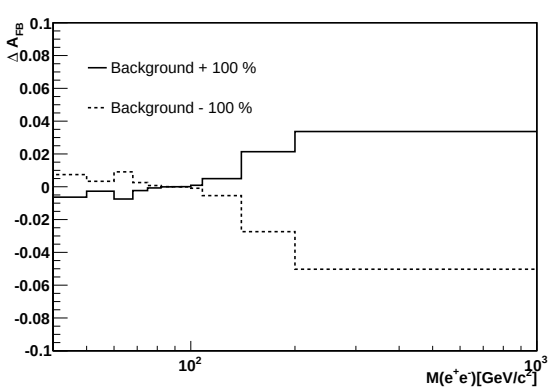

Figure 8.7: Systematic uncertainty of background subtraction in the electron channel.

8.5 Response Matrices

In unfolding procedure we use two dominant matrices, R_{FF} and R_{BB}. The effect of neglecting normalized R_{FB} and normalized R_{BF} on unfolding process is taken account of systematic uncertainty named response matrices.

In Figure 7.13, the mean A_{FB} is found in 12 mass regions using pseudo-experiments. The offset of the mean value from the expected A_{FB} is assigned as systematic uncertainty of response matrices as shown in Figure 8.8.

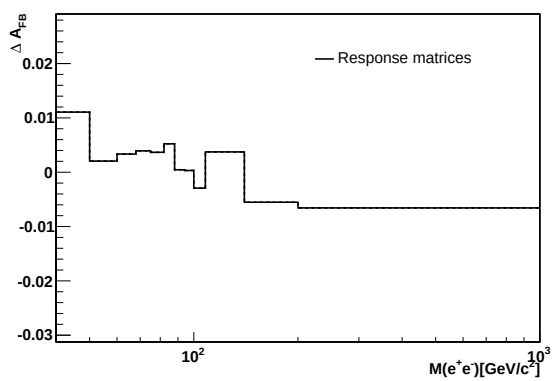

Figure 8.8: Systematic uncertainty of response matrices in the electron channel.

8.6 P_{T} of Dilepton

Data points in P_{T} of dilepton are slightly shifted compared to the MC as seen in Figure 7.1. Therefore, the effect of P_{T} of dilepton on A_{FB} is tested using event weighting. Then, systematic uncertainty of P_{T} of dilepton is assigned as difference of A_{FB} with weighting events from A_{FB} without weighting events (see Figure 8.9)

8.7 Quantum Electrodynamics (QED) Final State Radiation (FSR)

The FSR affects momentum and energy of lepton, and it induces mass bin migration. Figure 8.10 shows the energy difference between pre-FSR lepton and radiated lepton. The

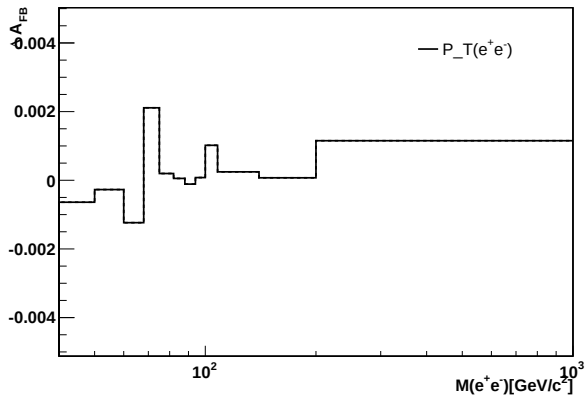

Figure 8.9: Systematic uncertainty of P_{T} of dilepton in the electron channel.

QED FSR tail events are defined where energy difference of pre-FSR lepton from radiated lepton is larger than 1 GeV. Since QED FSR is modeled by Pythia with 5% of systematic uncertainty [58], QED FSR uncertainties are defined by testing A^{t}_{FB} with reweighing 5 % up and down on the QED FSR tail events. Systematic uncertainty of FSR in the electron channel is shown in Figure 8.11.

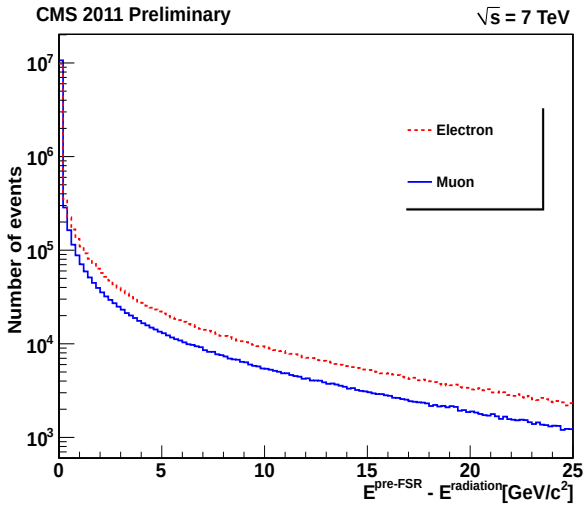

Figure 8.10: Energy difference between before and after QED FSR.

Table 8.2: The re-weighting factors for MC tuning on P_{T} of dilepton in the electron and muon channel.

$P_{\mathrm{T}}^{l^+l^-}$ [GeV/c]	dielectron	dimuon
1	1.33 ± 0.020	1.41 ± 0.020
2	1.27 ± 0.010	1.31 ± 0.009
3	1.18 ± 0.009	1.20 ± 0.007
4	1.08 ± 0.007	1.09 ± 0.006
5	1.01 ± 0.007	0.99 ± 0.005
6	0.96 ± 0.007	0.94 ± 0.005
7	0.92 ± 0.006	0.91 ± 0.005
8	0.91 ± 0.007	0.91 ± 0.005
9	0.91 ± 0.007	0.91 ± 0.006
10	0.91 ± 0.007	0.93 ± 0.006
11	0.91 ± 0.008	0.92 ± 0.006
12	0.93 ± 0.008	0.92 ± 0.007
13	0.93 ± 0.008	0.95 ± 0.007
14	0.94 ± 0.009	0.96 ± 0.007
15	0.96 ± 0.010	0.96 ± 0.008
16	0.95 ± 0.010	0.98 ± 0.008
17	0.97 ± 0.010	0.96 ± 0.008
18	0.99 ± 0.010	0.97 ± 0.009
19	0.97 ± 0.010	0.98 ± 0.009
20	0.98 ± 0.010	0.99 ± 0.010
>21	1.03 ± 0.003	1.01 ± 0.003

8.8 Mis-alignment

The muon momentum scale and resolution are affected by the reconstruction algorithms based on the track trajectory. However, the track momentum measurement has systematic uncertainties due to imperfect knowledge of the sub-detectors alignment and unknown effect of the detector material and the magnetic field. The uncertainties introduce inefficiency of charge and kinematic dependence. To correct the muon momentum, a function of Equation 8.2, is provided by the MuScleFit algorithm [59].

$$P_{\mathrm{T}}(New) = P_{\mathrm{T}} \times (1 + b \times P_{\mathrm{T}} + c \times Q_{\mu} \times P_{\mathrm{T}} \times \mathrm{sign}(\eta) \times \eta^2 + Q_{\mu} \times D \times P_{\mathrm{T}} \times \sin(\phi + E)) \tag{8.2}$$

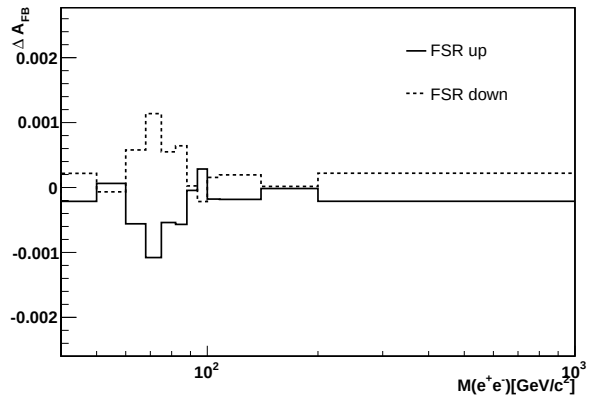

Figure 8.11: Systematic uncertainty of FSR in the electron channel.

where Q_μ is muon charge, and D, E = $d0, e0$, if $|\eta| < 0.9$, D, E = $d1, e1$, if $\eta > 0.9$, and D, E = $d2, e2$, if $\eta <$ -0.9. The parameters found with 759 pb^{-1} of 2011 data are listed in Table 8.3.

Table 8.3: The muon momentum correction parameters using the MuScleFit algorithm [60].

Parameters	value
b	-5.03313×10^{-6}
c	-4.41463×10^{-5}
$d0$	-1.48871×10^{-4}
$e0$	1.59501
$d1$	7.95495×10^{-5}
$e1$	-3.64823×10^{-1}
$d2$	1.52032×10^{-4}
$e2$	4.10195×10^{-1}

Figure 8.12 presents the mis-alignment uncertainty. The systematic uncertainty of mis-alignment in the muon channel is defined as a deviation on A_{FB} of with/without the MuScleFit correction in data. The MuScleFit correction is improved invariant mass agreement on data / MC as seen in Figure 8.13. However, the MuScleFit correction parameters are not used in this analysis because correction parameters should be applied to MC and data independently, and listed parameters for data are not optimized to the full data set of 2.2 fb^{-1}.

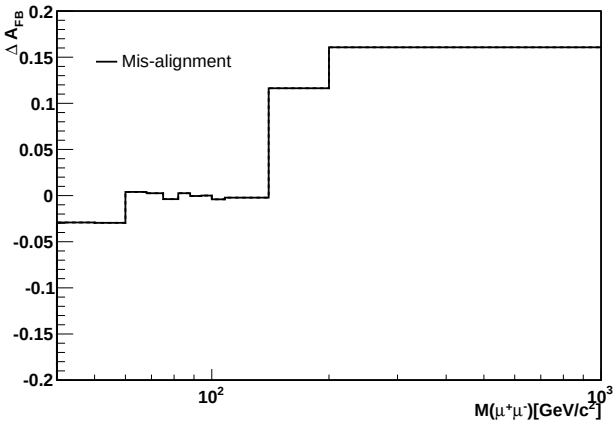

Figure 8.12: Systematic uncertainty of mis-alignment in the muon channel.

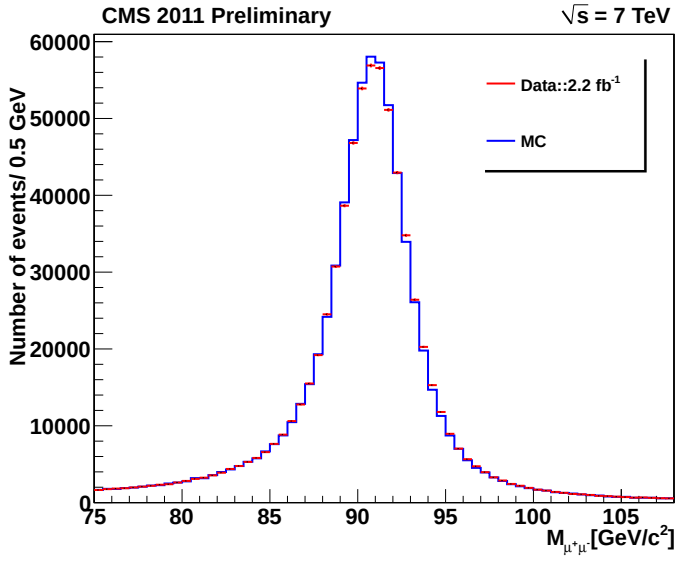

Figure 8.13: Invariant mass in data and MC with the MuScleFit correction.

8.9 Parton Distribution Functions (PDFs)

Systematic uncertainty of PDFs is adopted from [61]. Assigned PDFs uncertainties are 0.006, 0.008, 0.008, 0.007, 0.003, 0.002, 0.002, 0.003, 0.004, 0.007, 0.008, and 0.014 in 12 mass bins.

Table 8.4: Systematic error in the electron channel is listed in order of invariant mass of dimuon, pile-up (Pileup), efficiency (Effi), energy scale (Ecale), energy smearing (Eres), background (Bk), Response matrices (Mat), Transverse momentum of dilepton ($P_{\mathrm{T}}^{e^+e^-}$), QED FSR (FSR), and total systematic error (Sys.E).

$M_{e^+e^-}$	Pileup	Effi.	Escale	Eres	Bk	Mat	$P_{\mathrm{T}}^{e^+e^-}$	FSR	Sys. E
40-50	0.00861	0.00040	0.00463	0.00481	0.00741	0.01110	0.00063	0.00021	0.017
50-60	0.00209	0.00042	0.00256	0.00351	0.00333	0.00205	0.00027	0.00006	0.006
60-68	0.00149	0.00028	0.00137	0.00164	0.00908	0.00335	0.00124	0.00057	0.010
68-75	0.00181	0.00079	0.00916	0.00343	0.00256	0.00394	0.00211	0.00114	0.011
75-82	0.00152	0.00069	0.00918	0.00078	0.00075	0.00366	0.00019	0.00055	0.010
82-88	0.00491	0.00001	0.06140	0.00610	0.00006	0.00523	0.00005	0.00064	0.062
88-94	0.00039	0.00003	0.00071	0.00054	0.00001	0.00045	0.00011	0.00004	0.001
94-100	0.00025	0.00010	0.04810	0.00758	0.00005	0.00031	0.00007	0.00028	0.048
100-108	0.00169	0.00078	0.00211	0.00295	0.00091	0.00293	0.00102	0.00017	0.005
108-140	0.00538	0.00117	0.00359	0.00319	0.00540	0.00374	0.00024	0.00019	0.009
140-200	0.00429	0.00161	0.00154	0.00184	0.02740	0.00552	0.00007	0.00001	0.028
200-1000	0.00457	0.00161	0.00223	0.00173	0.05030	0.00657	0.00115	0.00022	0.051

Table 8.5: Systematic error in the muon channel is listed in order of invariant mass of dimuon, pile-up (Pileup), efficiency (Effi), energy scale (Ecale), energy smearing (Eres), background (Bk), Response matrices (Mat), Transverse momentum of dilepton ($P_{\mathrm{T}}^{\mu^+\mu^-}$), QED FSR (FSR), mis-alignment (Mis), and total systematic error (Sys.E).

$M_{\mu^+\mu^-}$	Pileup	Effi.	Escale	Eres	Bk	Mat	$P_{\mathrm{T}}^{\mu^+\mu^-}$	FSR	Mis	Sys.E
40-50	0.00194	0.00004	0.00082	0.00043	0.00056	0.00275	0.00031	0.00006	0.02910	0.029
50-60	0.00014	0.00003	0.00057	0.00009	0.00378	0.00250	0.00051	0.00003	0.02950	0.029
60-68	0.00557	0.00025	0.00008	0.00190	0.00602	0.00189	0.00093	0.00110	0.00397	0.009
68-75	0.00609	0.00009	0.00057	0.00295	0.00423	0.00101	0.00085	0.00241	0.00256	0.008
75-82	0.00088	0.00005	0.00082	0.00449	0.00073	0.00157	0.00102	0.00259	0.00384	0.006
82-88	0.00281	0.00029	0.00448	0.00660	0.00034	0.00087	0.00025	0.00102	0.00257	0.008
88-94	0.00015	0.00001	0.00039	0.00001	0.00000	0.00036	0.00002	0.00001	0.00043	0.001
94-100	0.00012	0.00015	0.00382	0.00499	0.00007	0.00100	0.00006	0.00015	0.00003	0.006
100-108	0.00110	0.00010	0.00104	0.00203	0.00070	0.00397	0.00001	0.00001	0.00405	0.006
108-140	0.00143	0.00032	0.00039	0.00103	0.00335	0.00118	0.00002	0.00021	0.00222	0.004
140-200	0.00784	0.00032	0.00116	0.00053	0.02290	0.00180	0.00012	0.00003	0.11600	0.119
200-1000	0.00221	0.00029	0.00040	0.00072	0.04180	0.00005	0.00092	0.00052	0.16100	0.166

Chapter 9

Conclusion

The forward-backward charge asymmetry of l^+l^- pair is measured with 2.2 fb^{-1} of pp collision data collected by CMS in 2011. The A_{FB} measurement is performed in a mass range between 40 GeV/c^2 to 1000 GeV/c^2, and the analyses include muons and electrons and their combination for the first time. Approximately, 0.8 million dimuons, 0.5 million central dielectrons, and 45 thousand electrons in the forward region are used in this analysis. The comparative studies between the experimental data and the simulated events are performed.

In order to perform the A_{FB} measurement, identifying quark direction is an important criterion, but the quark direction is unknown in the pp collisions. However, this ambiguity is highly reduced in the large rapidity range. The raw A_{FB}, measured in a large rapidity range of $|\eta| < 5$, with the electrons detected the forward calorimeters, provides nearly non-diluted A_{FB}.

We correct the raw A_{FB} for the detector mass resolution, kinematic and geometric acceptances, QED FSR, and the unknown quark direction because they constitute dilution factors. We adopt a matrix inversion method and unfold in three stages: limited pre-FSR, full pre-FSR, and non-diluted stages in order to obtain *true* A_{FB}. The uncorrected (raw) and corrected (unfolded) A_{FB} are consistent with the SM prediction within uncertainties.

Bibliography

[1] S. F. Novaes, "Standard Model: An Introduction", IFT-P.010/2000 (2000) arXiv:hep-ph/0001283v1.

[2] P. Drell, "Experimental Aspects of the Standard Model: A Short Course for Theorists", CLNS 96/1453, arXiv:hep-ex/9701001v1 (1997)

[3] C. Quigg, "Gauge Theories of the Strong, Weak, and Electromagnetic Interactions", Addison-Wesley (1983).

[4] D. H. Perkins, "Introduction to High Energy Physics", Cambridge University Press (2000).

[5] S. W. Herb *et al.*, "Observation of a Dimuon Resonance at 9.5 GeV in 400-GeV Proton-Nucleus Collisions", Phys. Rev. Lett. 39, 252-255 (1977).

[6] F. Abe *et al.*, "Observation of Top Quark Production in $\bar{p}p$ Collisions with the Collider Detector at Fermilab", Phys. Rev. Lett. 74, 2626-2631 (1995).

[7] DONUT Collaboration, "Observation of Tau Neutrino Interactions", FERMILAB-Pub-00/335-E, arXiv:hep-ex/0012035v1 (2000).

[8] UA1 Collaboration (G. Arnison et al.) "Experimental Observation of Lepton Pairs of Invariant Mass Around 95-GeV/c^2 at the CERN SPS Collider", Phys.Lett. B126, 398-410 (1983).

[9] UA2 Collaboration (P. Bagnaia et al.), "Evidence for Z0 —> e+ e- at the CERN anti-p p Collider", Phys. Lett. B129, 130-140 (1983).

[10] J. Womersley, "Beyond the Standard Model", Symmetry, Volume 02, issue 01, 22-25 (2005).

[11] J. L. Rosner, "Observability of charge asymmetries for lepton pairs produced in present collider experiment", Phys.Lett.B 221,85 (1989).

[12] J. L. Rosner, "Forward-backward asymmetries in hadronically produced lepton pairs", Phys.Rev.D 54,1078 (1996).

[13] N. Akchurin *et al.*, "Measurement of the Forward-Backward Asymmetry of $\mu^+\mu^-$ Pair in CMS at $\sqrt{s} = 7$ TeV" CMS AN 2010/455 (2010).

[14] N. Akchurin *et al.*, "Measurement of the Forward-Backward Asymmetry (A_{FB}) in $Z \to e^+e^-$ Events in CMS at $\sqrt{s} = 7$ TeV" CMS AN-2011/025 (2011).

[15] J. Lee, "A Measurement of the Z forward-backward charge asymmetry in p anti p $\to e^+e^-$", FERMILAB-THESIS-2006-88, UMI-32-45844 (2007).

[16] A. Bodek, "A simple event weighting technique: Optimizing the measurement of the forward-backward asymmetry of Drell-Yan dilepton pairs at hadron colliders", hep-ex:0911.2850v2 (2009).

[17] CDF Collaboration, Phys. Rev. D71, 052002 (2005).

[18] D-Zero Collaboration, PRL 101, 191801 (2008).

[19] Particle Data Group, Physics Letters B, Volume 667, 125 (2008).

[20] John F. Gunion, Howard Haber, Gordon Kane, Sally Dawson, "The Higgs Hunter's Guide", Addison-Wesley (1990).

[21] S. D. Drell and T. Yan, "Massive Lepton-Pair Production in Hadron-Hadron Collisions at High Energies" , Phys. Rev. Lett. 25, 316 (1970).

[22] http://indico.cern.ch/getFile.py/access?contribId=44&sessionId=1&resId=0&materialId=slides&confId=27439.

[23] J. C. Collins and D.E.Soper, "Angular distribution of dileptons in high-energy hadron collisions", Phys.Rev.D 16,2219 (1977).

[24] CMS Collaboration, JINST, 0803, S08004 (2008).

[25] http://www.physics.ucdavis.edu/∼conway/talks/TASI/Conway-TASI-1.pdf.

[26] M. Lamont, "LHC beam operations: past, present and future", http://moriond.in2p3.fr/QCD/2011/proceedings/lamont.pdf

[27] CMS collaboration, "The CMS magnet project: technical design report", CERN-LHCC-97-010, http://cdsweb.cern.ch/record/331056 (1997).

[28] A. Herve, "The CMS detector magnet", IEEE Trans. Appl. Supercond. 10, 389-394 (2000).

[29] CMS collaboration, "The CMS tracker system project: technical design report", CERN-LHCC-98-006, http://cdsweb.cern.ch/record/368412 (1998).

[30] CMS collaboration, "The CMS tracker: addendum to the technical design report", CERN-LHCC-2000-016, http://cdsweb.cern.ch/record/490194 (2000).

[31] CMS collaboration, "The electromagnetic calorimeter project: technical design report", CERN-LHCC-97-033, http://cdsweb.cern.ch/record/349375 (1997).

[32] CMS collaboration, "Addendum to the technical design report, Changes to the CMS ECAL Electronics", CERN-LHCC-2002-027, http://cdsweb.cern.ch/record/581342 (2002).

[33] CMS electromagnetic calorimeter group, "Results of the first performance tests of the CMS electromagnetic calorimeter", Eur. Phys. J. C44, s02, 1-10 (2006).

[34] CMS collaboration, "The hadron calorimeter project: technical design report", CERN-LHCC-97-031, http://cdsweb.cern.ch/record/357153 (1997).

[35] S. Abdullin *et al.*, "Design, performance, and calibration of CMS hadron-barrel calorimeter wedges", Eur. Phys. J. 55, 159-171, DOI: 10.1140/epjc/s10052-008-0573-yOpen Access (2008).

[36] S. Banerjee and S. Banerjee, "Performance of hadron calorimeter with and without HO", CMS-NOTE-1999-063, http://cdsweb.cern.ch/record/687178 (1999).

[37] N. Akchurin and R. Wigmans, "Quartz fibers as active elements in detectors for particle physics", Rev. Sci. Instrum. 74, 2955 (2002).

[38] CMS HCAL Collaboration, "Design, Performance and Calibration of the CMS Forward Calorimeter Wedges", Eur. Phys. J. C 53, 139-166 (2008).

[39] G. Abbiendi *et al.*, " Muon Reconstruction in the CMS Detector", CMS AN 2008/097 (2008)

[40] CMS collaboration, "The CMS muon project, technical design report", CERN-LHCC-97-032, http://cdsweb.cern.ch/record/343814 (1997).

[41] P. Nason,"A new method for combining NLO QCD with shower Monte Carlo algorithms", JHEP11, 040, arXiv:hep-ph/0409146, doi:10.1088/1126-6708/2004/11/040 (2004).

[42] S. Frixione, P. Nason, and C. Oleari, "Matching NLO QCD computations with Parton Shower simulations: the POWHEG method", JHEP 11, 070 arXiv:0709.2092, doi:10.1088/11266708/2007/11/070 (2007).

[43] S. Alioli, P. Nason, C. Oleari, and E. Re, "NLO vector-boson production matched with shower in POWHEG", JHEP 07, 06, arXiv:0805.4802, doi:10.1088/11266708/2008/07/060 (2008).

[44] T. Sjostrand, S. Mrenna , and P. Skands , PYTHIA 6.4 Physics and Manual, JHEP 0605,026, arXiv:hep-ph/0603175 (2006).

[45] H. Lai *et al.*, "New parton distributions for collider physics", Phys. Rev. D82, 074024, arXiv:1007.2241 (2010).

[46] J. Alwall *et al.*,"MadGraph/MadEvent v4: The New Web Generation", JHEP 09, 028, arXiv:0706.2334, doi:10.1088/1126-6708/2007/09/028 (2007).

[47] N. Davidson, G. Nanava, T. Przedzinski, E. Richter-Was, and Z. Was, "Universal Interface of TAUOLA Technical and Physics Documentation", IFJPAN-IV-2009-10, arXiv:1002.0543 (2010).

[48] S. Agostinelli *et al.*, "Geant4-simulation toolkit", NIM A 506/3, 250-303, doi:10.1016/S0168-9002(03)01368-8 (2003).

[49] J. Allison, K. Amako, and J. Apostolaskis *et al.*, "Geant4 developments and applications", IEEE Transactions on Nuclear Science 53/1, 270, doi:10.1109/TNS.2006.869826 (2006).

[50] https://twiki.cern.ch/twiki/bin/view/CMSPublic/SWGuideGsfElectronObject.

[51] W. Adam *et al.*, "Reconstruction of Electrons with the Gaussian-Sum Filter in the CMS Tracker at the LHC", CMS NOTE 2005/001 (2005).

[52] https://twiki.cern.ch/twiki/bin/view/CMS/SimpleCutBasedEleID.

[53] K.Klapoetke *et al.*,"Identification of Electromagnetic Particles in the Forward Hadron Calorimeter at CMS", CMS AN 2009/106 (2009).

[54] https://twiki.cern.ch/twiki/bin/view/CMSPublic/SWGuideFastSimPileUp.

[55] https://twiki.cern.ch/twiki/bin/viewauth/CMS/PileupMCReweightingUtilities.

[56] J. Berryhill *et al.*, "Electron Efficiency Measurement with 2.88 pb^{-1} of pp Collision Data at $\sqrt{s} = 7$ TeV" CMS AN 2010/349 (2010).

[57] G. Bauer *et al.*, "Fake Lepton Background Estimation for the $Z \to e^+e^-$ Cross Section Measurement Using the Fake Rate Method" CMS AN 2010/284 (2010).

[58] A. Kubik, "Studies of Final State Radiation in the Drell-Yan Di-Muon", CMS NOTE AN-11-044 (2011).

[59] S. Bolognesi *et al.*, "Calibration of track momentum using dimuon resonances in CMS" CMS AN-2010/059 (2010).

[60] https://indico.cern.ch/getFile.py/access?contribId=1&resId=0&materialId=slides&confId=128936

[61] E. Yazgan *et al.*, "Measurement of the Forward-Backward Asymmetry of l^+l^- Pairs in CMS at $\sqrt{s} = 7$", CMS AN 2011/356 (2011).